Physics – Uspekhi **58** (5) 419 – 445 (2015)

REVIEWS OF TOPICAL PROBLEMS

PACS numbers: 61.05.C –, **68.65. – k**

High-resolution X-ray diffraction in crystalline structures with quantum dots

V I Punegov

DOI: 10.3367/UFNe.0185.201505a.0449

Contents

Abstract. We review the current status of nondestructive high-resolution X-ray diffractometry research on semiconductor structures with quantum dots (QDs). The formalism of the statistical theory of diffraction is used to consider the coherent and diffuse X-ray scattering in crystalline systems with nanoinclusions. Effects of the shape, elastic strain, and lateral and vertical QD correlation on the diffuse scattering angular distribution near the reciprocal lattice nodes are considered. Using short-period and multicomponent superlattices as an example, we demonstrate the efficiency of data-assisted simulations in the quantitative analysis of nanostructured materials.

Keywords: high-resolution X-ray diffraction, coherent and diffuse scattering, superlattice, quantum dots

1. Introduction. Methods of research on structures with quantum dots

Quantum dot arrays in semiconducting systems find a wide range of applications in nano- and optoelectronics, including lasers, solar cells, transistors, emitters, and infrared photodetectors [1]. Therefore, the nondestructive control of the quantum dot (QD) shape, size, elastic strain, composition, and spatial distribution over large areas in growing epitaxial layers remains a major challenge.

Originally, semiconductor optoelectronics was based solely on heterostructures with ultrathin active layers (quantum wells) exhibiting dimensional quantization effects only in one direction [2]. The analysis of the quantization of higher-dimensional structures exemplified by quantum wires and QDs was initially undertaken theoretically [3], because structures with QDs proved more difficult to manufacture than quantum-well devices. Quantum dots were first observed experimentally in InAs/CaAs superlattices by transmission electron microscopy [4]. Parallel X-ray diffraction measurements [4] provided information only on the general superlattice structure. Because rocking curves (RCs) recorded with the help of a double-crystal diffractometer [4] characterize total X-ray scattering — including its coherent and diffuse components — data on the presence of QDs and the properties of nanostructures cannot be obtained based on the analysis of double-crystal RCs alone.

Transmission electron microscopy (TEM) [5] and cross-sectional scanning tunneling microscopy (X-STM) [6] are the well-known and widely used methods for studying QDs. TEM is employed to obtain information on QD size and ordering, as well as nanostructure contours, while X-STM makes measurements at the atomic level possible and thereby provides a deeper insight into the shape and composition of individual QDs. Unfortunately, both techniques are purely local and allow characterizing only very small portions of a sample; extrapolation of the data thus obtained to the whole sample requires great caution.

V I Punegov Komi Scientific Center,
Ural Branch of the Russian Academy of Sciences,
ul. Kommunisticheskaya 24, 167982 Syktyvkar, Russian Federation
E-mail: vpunegov@dm.komisc.ru

Received 9 January 2015, revised 8 February 2015
Uspekhi Fizicheskikh Nauk **185** (5) 449 – 478 (2015)
DOI: 10.3367/UFNr.0185.201505a.0449
Translated by Yu V Morozov; edited by A M Semikhatov

Another disadvantage of these methods is the necessity to destroy the sample by cleavage.

Methods based on X-ray diffraction provide data on the structural properties averaged over the entire sample. However, they also have drawbacks related first and foremost to their indirect character. This requires choosing an appropriate model for the construction of a relevant theory to be used as a basis for numerical simulation or the solution of the inverse X-ray diffraction problem [7–9]. Also important is the so-called phase problem, because the detector of an experimental setup fixes the complex reflection coefficient modulus, while the X-ray wave phase is lost.

Various approaches to the investigation of QD structural characteristics are based on the use of X-ray and synchrotron radiation. Grazing incidence small-angle X-ray scattering (GISAXs) [10, 11] is currently the most frequently used method for the purpose. It is rather simple as far as the study of QD shape and the treatment of its results are concerned. As a rule, GISAXS requires the use of intense synchrotron radiation (SR), because the signal in the form of a scattered X-ray wave is reflected from a QD itself rather than from a more massive matrix. Grazing incidence X-ray diffraction (DIXD) [11] is a more complicated method for the treatment of experimental data. In this case, X-ray diffraction originates in a crystalline matrix, whereas QDs play the role of structural defects.

Also worthy of mention are anomalous X-ray scattering methods, such as multiwavelength anomalous diffraction (MAD) and diffraction anomalous fine structure (DAFS) [12]. Methods using nanobeam X-ray diffraction (NBXD) [13] have been intensively developed in recent years. Finally, we mention methods of coherent X-ray scattering from QDs with the use of SR [14]. Most of the above X-ray experiments do not require developing sophisticated theories; numerical simulation is typically performed with the help of the finite element method [15]. Detailed analysis of small-angle and anomalous scattering techniques can be found in recent reviews [5, 10–12] and monographs [15–17]; practically all of them are realized with the help of SR sources, which hampers their wide application in modern material science research.

At the same time, there are no analytical reviews of research on crystalline systems with QDs based on the traditional methods of complanar high-resolution X-ray diffraction (HRXRD). This review is designed to fill this gap.

2. High-resolution X-ray diffraction

The use of X-rays for the solution of various diffraction problems implies in the first place the choice of an X-ray beam with a proper wavelength, monochromaticity, and angular spread. The majority of theories in the field of X-ray crystal optics are based on the assumption of an unbounded front of incident monochromatic radiation. This approach is not so simple in a real situation, because any radiation is characterized by spectral as well as angular spread. The use of perfect single crystals as monochromators and devices for beam formation in diffractometers ensures a high degree of radiation collimation and monochromatization ($\Delta\lambda/\lambda \sim 10^{-5}$). Specifically, the spread of a good synchrotron beam can be less than 1 arcsecond [15–18].

Recently, many diffraction studies have been carried out with the use of SR sources. The main advantages of SR include a continuous spectrum, high intensity and brightness, and a high degree of polarization and collimation along the beam length. Disadvantages (compared to an X-ray tube) are the low signal-to-noise ratio, difficulty of suppressing higher harmonics, and relatively low stability of radiation intensity [17, 18].

The small angular and spectral spread of the X-ray beam incident on the sample is achieved by a proper arrangement of crystal monochromators, collimators, and mirrors [18]. The beam spread can be decreased by using a crystal monochromator of asymmetric geometry with the diffraction planes not parallel to the crystal surface but making a certain angle φ with it. The beam angular width is narrowed by the choice of material for the monochromator crystal with a reduced susceptibility χ_h. Today, the most widely used materials for manufacturing monochromators are silicium and germanium crystals. Also, diamond is frequently used as a monochromator for SR due to its high resistance to radiation damage.

The use of X-ray optical elements allows forming beams with low divergence and high monochromaticity for diffraction experiments. Carefully choosing the collimator exit slit is equally important. The beam smearing and the results of measurements strongly depend on the slit width. Moreover, it is recommended that the so-called slotted multiple-reflection crystal monochromators proposed by Bonse and Hart be used [19].

On the other hand, suppression of multiple reflection 'tails' results in a large decrease in the reflection coefficient. Indeed, the resulting reflection curve obtained with a slot-type monochromator is the product of several curves, while the background intensity sharply decreases and the signal-to-noise ratio increases.

A double-crystal X-ray diffractometer consists of an X-ray radiation source, a monochromator, the studied sample, and a detector with a wide angular aperture. Such a device was proposed by Compton and Allison [20]. At present, it is sometimes called a double-axis diffractometer, because crystals are substituted by multilayer X-ray mirrors, or the monochromator may consist of a few crystals.

The use of a monochromator permits markedly decreasing the radiation spectral composition effect and generating a monochromatic linearly polarized beam of almost plane X-ray waves with a small angular spread.

During measurements by double-axis diffractometry, the X-ray beam reflected from the sample smears due to structural defects and instrumental distortions. To register the signal with a high angular resolution, the analyzer is placed between the sample and the detector. Such a setup with the rotating sample and analyzer is referred to as a triple-crystal X-ray diffractometer. Initially, such an instrument was called a triple-axis spectrometer [21], but the name triple-crystal diffractometer is presently more commonly used for the above reasons, bearing in mind the progress in X-ray optics.

2.1 Triple-axis X-ray diffractometry

The first design of a triple-axis diffractometer was realized in the study of thermal diffuse scattering in silicium, germanium, and diamond crystals in 1972 [21]. A year later, it was used to study dislocation loops and inclusions in copper by the Huang scattering method [22]. The modern interpretation of triple-axis diffractometry is expounded in Ref. [23].

In this method, the monochromator and the analyzer are perfect single crystals in a parallel and dispersion-free configuration $(n, -n, +n)$. Registered RCs are termed 'scans' in the ω-, ε-, and $\theta/2\theta$-section mode of the reciprocal $\mathbf{q}(\omega, \varepsilon)$

space, depending on the relative rotation of the sample and the analyzer.

The reflection intensity $I_h(\mathbf{q})$ is a function of the rotation angles of the sample, ω, and the analyzer, ε. Therefore, the reciprocal space map (RSM) of the scattering intensity angular distribution shows equal-intensity contours $I_h(\mathbf{q}) = I_h(\omega, \varepsilon) = \text{const}$. To construct it in rectangular (q_x, q_z) or oblique (ω, ε) coordinates, measurements of scattering intensity from the sample should be made with a given angular resolution by recording a number of sections $I_h(q_x, q_z)$ or $I_h(\omega, \varepsilon)$.

An RSM formation scheme for the study of defective crystals is presented in Ref. [23]. RSMs of the scattering intensity angular distribution are constructed near a reciprocal lattice (RL) node **h** belonging to crystal reflecting planes (hkl). The scattering vector $\mathbf{Q} = \mathbf{k}_h - \mathbf{k}_0$ is usually represented as the sum $\mathbf{Q} = \mathbf{h} + \mathbf{q}$, where the vector **q** is the deviation of the scattering vector from the RL node. In a symmetric diffraction scheme, projections of **q** in the diffraction plane are determined by the angular positions of the sample and the analyzer: $q_x = \kappa \sin\theta_B(2\omega - \varepsilon)$ and $q_z = -\kappa \cos\theta_B\, \varepsilon$, where θ_B is Bragg's angle. It follows from these relations that in symmetric diffraction geometry, only q_x changes under sample rotation, and the space in the direction perpendicular to the RL vector **h** is analyzed.

Rotating the analyzer crystal through ε affects both q_z and q_x, giving an intensity distribution over the Ewald sphere. The condition $q_x \equiv 0$ must be satisfied for the movement along **h**, which leads to $2\omega = \varepsilon$. The analyzer scanning rate is twice the sample rotation velocity; such scanning is usually termed $(\omega{-}2\theta)$ or $\theta/2\theta$ scanning. Sample deviation from the initial position when the analyzer is motionless (ω-scanning) corresponds to the RL rotation around the origin and therefore the end of the vector **h** describes an arc around the (000) node.

Sectioning far from the RL node as a result of rotation of the sample crystal (for instance, at a fixed position of the analyzer crystal) gives the intensity distribution along the line $\varepsilon = \text{const}$. In this case, the curve has three peaks called the analyzer pseudopeak, the main peak, and a monochromator pseudopeak at the respective angular positions $\omega = 0$, $\omega \approx \varepsilon/2$, and $\omega = \varepsilon$. In a different method of scanning, when the analyzer rotates and the sample remains fixed ($\omega = \text{const}$), there are two peaks besides the diffuse background: the monochromator pseudopeak at $\varepsilon = \omega$ and the main peak at $\varepsilon = 2\omega$. In recording $(\omega{-}2\theta)$ or $\theta/2\theta$ scanning, we are dealing with a section of the reciprocal space along the **h** vector (Bragg scattering), the peak at a single point $\omega = \varepsilon = 0$, and the total RC profile recorded at $\varepsilon = 2\omega$.

The form of RSMs depends not only on the study sample but also on the monochromator and analyzer type. With these X-ray optics elements produced with regard for multiple reflection, pseudopeak intensities in the diffraction pattern markedly decrease and can even disappear [24]; hence, the importance of the problem related to the influence of instrumental distortions on the formation of RSMs of the scattering intensity angular distribution [25–27].

2.2 Statistical theory of X-ray diffraction. Coherent and diffuse scattering

X-ray scattering from structures with QDs is typically described in terms of one variant or another of statistical diffraction theory, such as the one based on the use of the Kato formalism [28–40], the mutual coherence function [41, 42], and the Dederichs–Krivoglaz kinematic approach [43, 44]. Interpretation in the framework of Kato's statistical dynamical theory [28] describing both coherent and diffuse scattering as a whole appears to be the most promising, albeit a more complicated approach. Other methods [41–43] allow analyzing diffuse scattering only separately from the coherent part, and are therefore applicable only at large values of q_x and q_z, when the influence of the coherent component can be neglected.

The construction of a consistent triple-crystal diffractometry theory presents serious challenges, one of which is related to the intensity normalization. In a theoretical treatment, the incident plane wave usually has an infinite intensity, while the intensity of a diffusely scattered wave remains finite. The intensities of coherent and diffuse waves become incomparable. On the other hand, the intensity of an experimental primary beam from the monochromator illuminates only a certain part rather than the entire surface, depending on the exit slit width. Therefore, a theoretical description of the intensity of an X-ray beam incident on the sample should relate it to its lateral width and regard the intensity as a finite value.

One more problem arises in experimental differentiation between coherent and diffuse scattering intensities. These intensities overlap in the immediate vicinity of the RL node, which means that ignoring distribution patterns of the coherent and diffuse components makes it difficult to obtain information about the structural characteristics of the study object.

It was noted above that the formalism of the statistical dynamical theory of spherical wave diffraction from a defective crystal was proposed by Kato [28]. This theory was modified by Bushuev in the case of a plane wave [29, 30]. For gradient and multilayer crystals, the formalism of statistical dynamical theory was developed in Refs [31–40]. Specifically, a variant of the one-dimensional statistical dynamical diffraction theory was applied to study laser heterostructures by the combined analysis of double- and triple-crystal RCs in the $\theta/2\theta$ scanning mode [7]. The same method was used in the numerical solution of the inverse problem of diffraction from gradient semiconductor structures [8, 9]. However, it is impossible to analyze RSMs in the framework of these theories.

The general case of the statistical dynamical theory for triple-crystal diffractometry is described in Ref. [37]. This theory applies to crystals of any thickness, but the main equations unfortunately have a very complicated mathematical structure. It was shown in Refs [35, 45] that the effects of diffuse absorption of coherent waves, multiple diffuse scattering, and Bragg's diffraction of diffuse waves can be neglected for crystals less than 10 μm thick. Bearing this in mind, the theory in [37] was modified for the description of X-ray scattering in layers and films with a thickness up to 10 μm [40]. The modified theory considers coherent scattering in the framework of dynamical diffraction and diffuse scattering, taking only primary extinction into account. Multiple diffuse scattering or, in other words, secondary extinction is disregarded, because it has practically no influence on the diffraction pattern.

Various defects in real crystalline structures disturb the ideal lattice periodicity. Because these disturbances are random, e.g., result from the presence of randomly distributed inhomogeneities in the bulk, X-ray diffraction is inevitably accompanied by diffuse scattering. In this review,

self-organized QDs are regarded as a certain type of defect of the crystalline structure arising from the mismatch between lattice parameters of QDs and the basic matrix. Moreover, it should be borne in mind that the size of nanostructures and their spatial correlation characteristics are subject to inevitable fluctuations.

We note that a distortion of the ideal periodicity of the crystal lattice may be nonrandom, as in the case of elastic bending of the sample. Such distortion is described by a continuous lattice displacement field $\mathbf{u}(\mathbf{r})$. In the presence of defects in a crystalline structure, the lattice displacement function $\mathbf{u}(\mathbf{r})$ [and hence the phase function $\phi(\mathbf{r}) = \exp(\mathrm{i}\mathbf{h}\mathbf{u}(\mathbf{r}))$] is represented in the form of the mean and fluctuation parts,

$$\mathbf{u}(\mathbf{r}) = \langle \mathbf{u}(\mathbf{r}) \rangle + \delta\mathbf{u}(\mathbf{r}) , \qquad \phi(\mathbf{r}) = \langle \phi(\mathbf{r}) \rangle + \delta\phi(\mathbf{r}) ,$$

where $\langle \phi(\mathbf{r}) \rangle = \exp(\mathrm{i}\mathbf{h}\langle \mathbf{u}(\mathbf{r}) \rangle)$ describes nonrandom large-scale strains in the bulk crystal. Random lattice displacements caused by statistically distributed defects are given by the fluctuation phase function $\tilde{\phi}(\mathbf{r}) = \exp(\mathrm{i}\mathbf{h}\,\delta\mathbf{u}(\mathbf{r}))$; its mean $f(\mathbf{r}) = \langle \tilde{\phi}(\mathbf{r}) \rangle$ is defined as the Debye–Waller static factor [28].

X-ray diffraction in imperfect crystals is described by a set of coupled Takagi equations [46] for transmitted $E_0(\mathbf{r})$ and diffraction $E_h(\mathbf{r})$ wave amplitudes. These equations are widely used to analyze RCs in double-crystal geometry. A transition from double- to triple-axis diffractometry requires certain mathematical transformations, resulting in the substitution of the initial amplitudes $E_{0,h}(\mathbf{r})$ by their Fourier transforms $E_{0,h}(q_x, y, z)$ in the diffraction equations. The next step is statistical averaging of the diffraction equations, owing to which the X-ray field amplitudes are represented as the sum of coherent $\langle E_{0,h}(q_x, y, z) \rangle = E^{\mathrm{c}}_{0,h}(q_x, y, z)$ and diffuse $\delta E_{0,h}(q_x, y, z) = E^{\mathrm{d}}_{0,h}(q_x, y, z)$ components.

The following equations describing coherent scattering have been derived in statistical X-ray diffraction theory [40]:

$$\begin{cases} \dfrac{\partial E^{\mathrm{c}}_0(q_x, y, z)}{\partial z} = \mathrm{i}(a_0 - q_x \cot\theta_1) E^{\mathrm{c}}_0(q_x, y, z) \\ \quad + \mathrm{i}\,\dfrac{a_{-h} f}{\sqrt{2\pi}} \displaystyle\int_{-\infty}^{+\infty} \mathrm{d}q'\, E^{\mathrm{c}}_h(q_x - q', y, z)\, \bar{\phi}(q', y, z) , \\ -\dfrac{\partial E^{\mathrm{c}}_h(q_x, y, z)}{\partial z} = \mathrm{i}(b a_0 + \eta - q_x \cot\theta_2) E^{\mathrm{c}}_h(q_x, y, z) \\ \quad + \mathrm{i}\,\dfrac{a_h f}{\sqrt{2\pi}} \displaystyle\int_{-\infty}^{+\infty} \mathrm{d}q'\, E^{\mathrm{c}}_0(q_x - q', y, z)\, \bar{\phi}^*(q', y, z) , \end{cases} \tag{1}$$

where $a_0 = \pi\chi_0/(\lambda\gamma_0)$, $a_{h,-h} = C\pi\chi_{h,-h}/(\lambda\gamma_{h,0})$, $\eta = (2\pi/\lambda\gamma_h)\sin(2\theta_{\mathrm{B}})\omega$ is the angular parameter used in double-crystal diffractometry in the $\theta/2\theta$ scanning mode, λ is the X-ray wavelength in a vacuum, $\omega = \theta - \theta_{\mathrm{B}}$ is the deviation of the X-ray beam from the Bragg angle θ_{B}, $\gamma_{0,h} = \sin\theta_{1,2}$, $\theta_{1,2} = \theta_{\mathrm{B}} \mp \varphi$ are the angles determining the direction of the incident and diffraction beams relative to the entrance surface of the crystal, φ is the tilting angle of the reflecting planes with respect to the sample surface, $b = \gamma_0/\gamma_h$ is the asymmetry factor, C is the polarization factor, $\chi_{0,h} = -r_0(\lambda^2/\pi V_{\mathrm{c}})F_{0,h}$ is the Fourier component of X-ray polarization, V_{c} is the unit cell volume, $r_0 = e^2/(mc^2)$ is the classical electron radius, e and m are the electron charge and mass, and $F_{0,h}$ are the structural factors in the direction of transmission and diffraction. For the purpose of describing X-ray scattering in the context of triple-axis diffractometry, the angular parameter η is written in terms of projections of the vector $\mathbf{q}$ as $\eta = q_x \cot\theta_2 - q_z$. The parameters $\bar{\phi}(q', y, z)$ and $\bar{\phi}^*(q', y, z)$ in the right-hand side of Eqns (1) are Fourier transforms of the phase functions $\bar{\phi}(\mathbf{r})$ and $\bar{\phi}^*(\mathbf{r})$, where the asterisk denotes complex conjugation.

In general, both diffuse and coherent scatterings occur in the complicated process of dynamical diffraction and are described by a set of integro-differential equations [37]. Semiconducting crystals of opto- and nanoelectronics are usually investigated in Bragg's geometry; therefore, diffuse scattering can be described in the kinematic (Born) approximation, ignoring secondary extinction, which substantially simplifies the analysis.

We consider the diffuse scattering intensity distribution near a reciprocal lattice node $\mathbf{h}$ as a function of the vector $\mathbf{q}$. By definition, the diffuse scattering intensity on the crystal surface is expressed as [28, 44]

$$I^{\mathrm{d}}_h(\mathbf{q}) = \langle E_h(\mathbf{q})\, E^*_h(\mathbf{q}) \rangle - \langle E_h(\mathbf{q}) \rangle \langle E^*_h(\mathbf{q}) \rangle . \tag{2}$$

The first term in the right-hand side of Eqn (2) stands for the total scattering intensity, from which the coherent component is subtracted. The use of the formal solution for coherent waves (1) and simple transformations of the statistical dynamical diffraction theory [28] yield an equation for the diffuse scattering angular distribution:

$$I^{\mathrm{d}}_h(\mathbf{q}) = \int_0^l \mathrm{d}z \int \mathrm{d}x \int \mathrm{d}y\, |a_h(\mathbf{r})|^2 \big(1 - f^2(\mathbf{r})\big) \times \exp\big[-(1+b)\,\mu z\big]\, \tau(\mathbf{r}, \mathbf{q})\, I^{\mathrm{c}}_0(\mathbf{r}) , \tag{3}$$

where μ is the linear X-ray absorption coefficient and $I^{\mathrm{c}}_0(\mathbf{r})$ is the intensity of the transmitted X-ray beam within the bulk of the crystal at the point with a coordinate $\mathbf{r}$.

Relation (3) for the diffuse scattering intensity is applicable to crystalline media undergoing spatial changes in the chemical composition, structural defects, and extended elastic strains of the crystal lattice. This formula coincides with the expression for incoherent scattering intensity from one-dimensionally deformed crystals in a double-axial recording scheme [31–33]. The two expressions differ in that Eqn (3) contains the correlation volume instead of the correlation length [37, 38, 40]:

$$\tau(\mathbf{r}, \mathbf{q}) = \int_{-\infty}^{+\infty} \mathrm{d}\boldsymbol{\rho}\, g(\mathbf{r}, \boldsymbol{\rho}) \exp\Big[\mathrm{i}\big(\mathbf{q}\boldsymbol{\rho} + \mathbf{h}\big(\langle \mathbf{u}(\mathbf{r} + \boldsymbol{\rho}) \rangle - \langle \mathbf{u}(\mathbf{r}) \rangle\big)\big)\Big] , \tag{4}$$

where the vector $\boldsymbol{\rho}$ determines the shift from a given point $\mathbf{r}$. This parameter characterizes the diffuse scattering intensity angular distribution in deformed crystals and depends on the structural defects distributed in the bulk. The type of defects (shape, size, elastic strains, etc.) is described by the intrinsic correlation function [28, 38]

$$g(\mathbf{r}, \boldsymbol{\rho}) = \frac{\big\langle \exp\big[\mathrm{i}\mathbf{h}\big(\delta\mathbf{u}(\mathbf{r} + \boldsymbol{\rho}) - \delta\mathbf{u}(\mathbf{r})\big)\big] \big\rangle - f^2(\mathbf{r})}{1 - f^2(\mathbf{r})} . \tag{5}$$

An analytic expression for the intrinsic correlation function has been derived for certain defect models in Refs [38, 39, 47, 48]. Considering diffuse scattering in the framework of triple-axis diffractometry implies integrating (4) over q_y. This results in transforming the correlation volume into the correlation area $\tau(\mathbf{r}, q_x, q_z) = \int_{-\infty}^{+\infty} \mathrm{d}q_y\, \tau(\mathbf{r}, \mathbf{q})$ [38, 39]. For a uniform distribution of defects, the solution for the correla-

tion volume can be represented in a different form. Introducing the function $D(\mathbf{r}) = 1 - \exp(i\mathbf{h}\,\delta\mathbf{u}(\mathbf{r}))$ [49] allows writing the expression for the Debye–Waller factor as

$$f = \exp\left(-\frac{c}{V_c}\int D(\mathbf{r})\,d\mathbf{r}\right).$$

Moreover, intrinsic correlation function (5) can be represented in the form

$$g(\boldsymbol{\rho}) = c\left[V_c(1-f^2)\right]^{-1}\int D(\mathbf{r})\,D^*(\mathbf{r}+\boldsymbol{\rho})\,d\mathbf{r},$$

where c is the concentration of defects in the bulk crystal. The introduction of the spatial-variable function $D(\mathbf{r})$ facilitates practical calculations. Specifically, the expression for the correlation volume can be represented using the Fourier transform $D(\mathbf{q}) = \int D(\mathbf{r})\exp(i\mathbf{q}\mathbf{r})\,d\mathbf{r}$:

$$\tau(\mathbf{q}) = c\left[V_c(1-f^2)\right]^{-1}\left|D(\mathbf{q})\right|^2. \quad (6)$$

Because the intensity angular distribution in Eqn (3) is proportional to the correlation volume, the parameter $D(\mathbf{q})$ in (6) can be logically interpreted as the diffuse scattering amplitude. The representation of $\tau(\mathbf{q})$ in form (6) has been used to calculate diffuse scattering from crystalline media with spherically symmetric defects [50], quantum dots [51, 52], and quantum rings [53].

2.3 Direct and inverse X-ray diffraction problems

The development of the theory and the choice of the solid structure model as a basis for the calculation of the scattering intensity angular distribution are commonly regarded as the direct problem of X-ray diffractometry. Modern experimental X-ray diffraction measurements are frequently accompanied by numerical simulation. Researchers are satisfied with a qualitative coincidence of theoretical and experimental data in the framework of the solution of the direct problem.

A specific aspect of X-ray diffraction optics is the solution of inverse problems for the structured medium parameters based on X-ray diffraction data [7–9, 54–61]. Various approaches to the reconstruction of structural characteristics of materials include high-resolution X-ray diffractometry [7, 54–58], reflectometry [59, 60], and the phase contrast technique [61]. Analysis of X-ray rocking curves (see [54] and the references therein) provides information on the crystal lattice strain profile, composition, and static Debye–Waller factor. Difficulties in uniquely determining the lattice composition and structural defects arise as early as this stage, because diffraction equations contain the product of Fourier coefficients of the medium polarizability and the static Debye–Waller factor, which are jointly responsible for the degree of interaction between X-ray waves and the electronic system of the medium under conditions of Bragg's diffraction. Additional diffraction measurements and data obtained by other methods are needed to eliminate the ambiguity. For example, the results of double- and triple-crystal diffractometry were used for the numerical solution of the inverse problem in Ref. [7], whereas the authors of [58] analyzed different orders of diffraction reflection.

The solution of the inverse problem has some peculiarities. Because the inverse problem involves the solution of differential, integral, and integro-differential equations, the well-posedness of the problem acquires special importance [54]. The existence of the solution, its uniqueness, and its stability are to be considered in the first place. A necessary condition for well-posedness is the phase problem, because the diffractometer detector fixes the complex reflection coefficient modulus, but the phase is lost. Moreover, in solving the inverse X-ray diffraction problem, peculiarities of a given experiment with its inevitable measurement errors and instrumental distortions imposed on the signal must be taken into account. Taken together, these factors virtually prevent a unique solution of the inverse problem.

The diffraction problem becomes much more complicated if the studied object contains statistically distributed inclusions in the crystalline space. We note that these inclusions practically always differ in size; therefore, it makes no sense to speak of the absolute uniqueness of the solution. It is in principle impossible in the near future to obtain information on the size and spatial arrangement of individual nanoinclusions in a structured medium, even with the use of ultrapowerful supercomputers. For the present, only averaged characteristics of a study object are available for analysis.

In contrast to X-ray reflectometry [60], in which interaction of X-ray waves depends on the electron density of the medium, an indispensable condition for X-ray diffractometry is translational ordering of atoms in the crystal lattice. We note that crystalline systems with an ideal structure and periodically distributed homogeneous nanoinclusions are thus far unavailable, despite recent progress in crystal growth technology; therefore, production of coherent X-ray waves in the diffraction process is always accompanied by diffuse scattering. Such scattering is characterized by the specific intensity angular distribution, depending on the nanostructure size and shape; it is superimposed on the coherent component and thereby contributes to the total signal. This creates a serious obstruction to the solution of model-independent inverse problems.

Nevertheless, the solution of inverse problems based on minimizing the residual functional describing how closely calculations conform to observed data in the framework of the chosen model allows obtaining sufficiently accurate information on the structural characteristics of the study objects.

3. X-ray diffraction in structured media

Structured crystalline media encompass solid-state systems and multilayer structures characterized not only by a translational period of the basic matrix but also by an additional period or other spatial variation resulting from the use of modern technologies or external impacts. Such objects include single crystal and multilayer surface gratings, nanoporous layers, semiconducting superlattices, self-organized systems with quantum dots and wires, etc. Results of high-resolution X-ray diffractometry of nanostructured media, including self-organized quantum wires, correlated surface roughnesses, etc., on the lateral surface and in the bulk of the lattice are reported in Ref. [62]. Most experiments with these objects were carried out in a grazing geometry and calculations are made in the distorted-wave Born approximation.

3.1 Multilayer quantum dots

We consider the application of high-resolution X-ray diffractometry for the study of structures with QDs. First, RSMs of the X-ray scattering intensity angular distribution were used to analyze multilayer GaAs/AlAs QDs obtained by electron-beam lithography with subsequent ion etching [63–

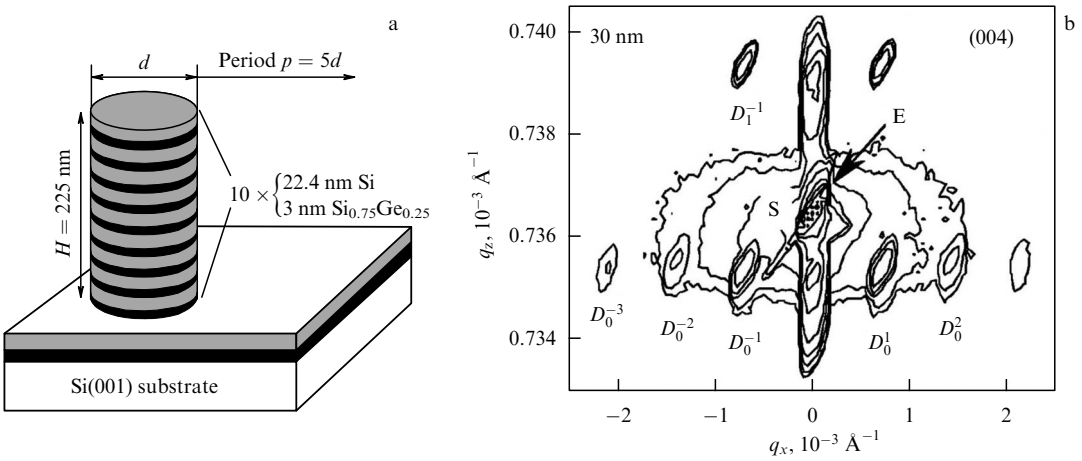

Figure 1. Schematic of (a) a multilayer QD and (b) an RSM from a lateral periodic structure from Si/SiGe quantum dots [67].

66]. Contours of equal intensity measured for (004) and (113) RL nodes produced a picture of satellites periodically arranged in vertical and lateral directions. The multilayer nanostructures were much bigger than self-organized QDs; electron microscopy showed that they were shaped like cylinders 640 nm in height having a radius of 65 nm. Such QDs formed a two-dimensional lateral lattice with a period of 350 nm in one direction and 300 nm in the other (perpendicular) direction.

A two-dimensional model for calculating coherent and diffuse scattering was proposed for the quantitative analysis of QD structural characteristics and lateral ordering [64]. A comparison of numerical results and experimental data yielded averaged structural characteristics of QDs, such as the mean strain values in nanostructures and their size averaged over the ensemble. X-ray diffraction measurements, showed that the mean QD radius was 50 nm instead of the 65 nm on electron micrographs [64]. Analyses of diffuse scattering revealed random lattice shifts in the bulk multilayer QDs. The formation of a diffuse spot around the GaAs node can be attributed to the presence of defects in the substrate near-surface layer. The cause of a much stronger diffuse scattering for asymmetric diffraction than (004) reflection remains to be explained. The authors of Ref. [64] argue that the numerical simulation results generally agree with experimental data for RSMs from laterally ordered multilayer QDs.

The results of a later study on multilayer QDs in Si/SiGe by the HRXRD method are reported in Ref. [67]. The original superlattice of Si/SiGe with quantum wells was grown using the molecular beam epitaxy technique at 600 °C. A laterally periodic structure was formed from QDs by electron lithography with subsequent ion beam etching. Certain QD samples were cylinders with a radius of 30, 40, 60, or 100 nm (Fig. 1a).

Similar to previous studies [63–66], RSMs of multilayer Si/SiGe QDs showed additional diffraction orders (satellites) in the vertical and lateral directions (Fig. 1b). The relatively large angular dimension of satellites on the RSMs is due to the use of a wide detector slit for the enhancement of scattering intensity. The symbol S in Fig. 1b denotes the diffraction peak from the substrate and D_i^j indicates the corresponding diffraction order (satellite), where the subscript i is the superlattice diffraction order and the superscript j is the lateral order related to the QD periodic arrangement. Line E is the trace of the Ewald sphere in the plane of reciprocal space due to the limited angular resolving power of the diffractometer detector. The processes of elastic relaxation in bulk multilayer Si/SiGe QDs were studied based on X-ray diffraction data and calculations by finite element methods [67].

3.2 Semiconductor structures with self-organized quantum dots

The first observation of the growth of self-organized InGaAs QDs in the InAs/GaAs SL structure dates back to 1985 [4]. The results of high-resolution X-ray diffractometry were used for the quantitative analysis of Si/Ge structures with QDs only 10 years later [68]. The angular distribution of scattering intensity from superlattices with self-organized QDs near RL nodes in SeGe [68–72] and InGaAs [73–77] suggested the presence of interference diffuse maxima around superstructural satellites of coherent scattering (Fig. 2).

The statistical kinematic X-ray diffraction theory was used for RSM numerical simulation [69, 70] to obtain information on elastic strains and the vertical and lateral correlation of the QDs. The authors of Refs [69, 70] calculated diffuse scattering using a cylindrical QD model. Elastic strain fields associated with the presence of QDs in the crystalline

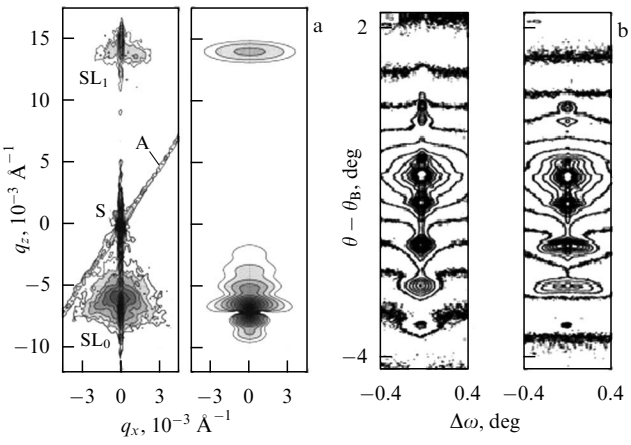

Figure 2. (a) Measured (left) and simulated RSM near the (004) node of the Ge/Si superlattice with SiGe QD [70]; (b) measured RSM near the (004) node of the InAs/GaAs superlattice with InGaAs QDs for different azimuthal positions of the sample [77].

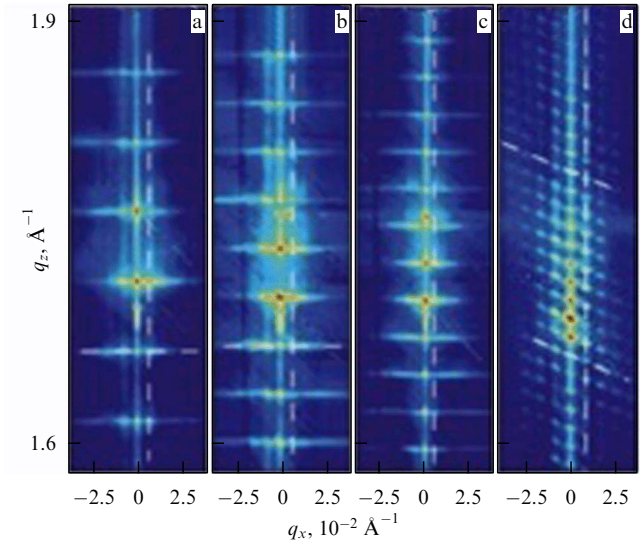

Figure 3. RSM (111) reflections from PbSe/PbEuTe superlattices with different thicknesses of PbEuTe spacers: (a) 10.4 nm, (b) 16.4 nm, (c) 21.4 nm, (d) 45.4 nm. Formation of a 3D hexagonal lattice from QDs (a–c), and 3D trigonal lattice from QDs (d) [80].

medium were calculated with the use of Green's functions. Only qualitative agreement between the results was achieved (Fig. 2a), because only the diffuse component was taken into account to compare experimental and theoretical RSMs in the framework of the computational algorithm. Nonetheless, Refs [69, 70] demonstrated the unique potential of the HRXRD method for the study of morphology and elastic strain in structures with self-organized QDs.

The method for RSM construction was later successfully used for the analysis of PbSe/PbEuTe [78–80], EuTe/SnTe [81], InAs/InP [82], and ZnMgTe/ZnSe [83] multilayer systems with QD arrays. For example, the authors of Ref. [80] showed that the PbSe/PbEuTe lattice is unique in that a variety of interlayer correlations are formed in it depending on changes in the PbEuTe spacer thickness, the PbSe QD size, and the growth temperature. Figure 3 shows RSM (111) reflections from PbSe/PbEuTe superlattices differing in the spacer thickness. When the spacer thickness is relatively small, the QDs form a 3D hexagonal lattice in which they are arranged strictly one above the other in the vertical direction. The presence of a thick spacer layer results in the formation of a 3D trigonal lattice from QDs with a nonvertical line, whose slope is found from the RSM analysis (see Fig. 3). Well apparent vertical diffraction satellites can be observed together with lateral oscillations of the scattering intensity distribution caused by the short-range ordering of QDs in the horizontal direction [80].

A diffuse scattering angular distribution on the RSM permits determining not only the QD size, elastic strain, and spatial correlation, but also the stacking slope, i.e., deviation from the QD vertical arrangement one after another relative to the sample surface [80, 84–86]. We also note that the RSM method is successfully used to study the morphology of QD chains by measurements at different azimuthal positions of the sample [87, 88].

3.3 Diffraction on 3D periodic quantum dot arrays

Modern nanotechnologies allow creating new artificial materials with various functional properties for devices to be

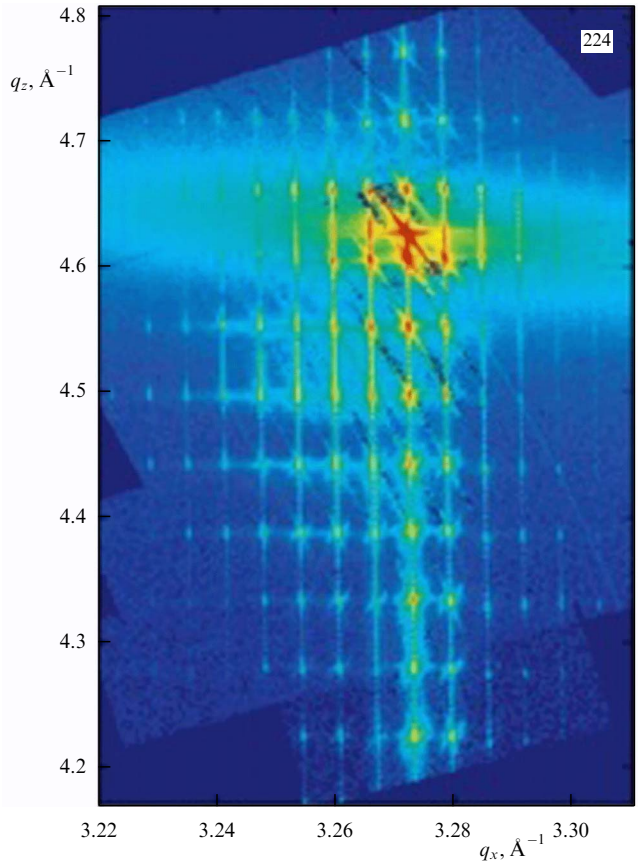

Figure 4. RSMs near the (224) Bragg peak from a 3D SiGe QD periodic structure [90].

used in physics, chemistry, biology, and medicine. Self-organization of nanostructures with the use of templates is recognized as a possible method for the precise positioning of nanoscale objects to obtain arrays, molecules, and crystals from QDs.

High-resolution X-ray diffractometry was used to determine the size, chemical composition, and strains of self-organized Ge/Si(001) islands in the form of a 3D lattice grown on a (001)Si substrate with pits preliminarily etched by electron-beam lithography and arranged in the form of a square grid [89]. Numerical simulation of the measured diffuse scattering intensity was performed in the framework of the kinematic approximation in order to determine the island parameters. To create templates with a desired periodicity and reduce the structure size, UV interference lithography (EUV-IL) at the wavelength 13.5 nm was used [90].

The structural perfection of a 3D Si/SiGe periodic system was investigated by high-resolution diffractometry with the use of synchrotron radiation [89]. RSMs near (004) and (224) reciprocal lattice nodes were measured and analyzed to obtain quantitative information on positional distortions in the QD arrangement and to determine Ge content in the QDs. The authors proposed a structural model describing elastic strain depending on the QD shape and composition with the QD spatial distribution taken into account [91]. A typical RSM with a well apparent structure of numerous diffraction satellites in vertical and lateral directions inherent to long-range objects is shown in Fig. 4 [90].

4. Influence of the quantum dot shape, size, and elastic strain on X-ray diffuse scattering

Of all the characteristics of nano-scale structures in a crystalline medium, the shape, size, and elastic strain caused by the mismatch between QD lattice parameters and the matrix material play the most important role. Specifically, the elastic strain is responsible for a marked alteration of the electron zonal structure of the material. Moreover, it plays a special role in the process of spatial ordering of QDs in semiconducting materials.

Much attention has recently been given to research on the elastic strain distribution inside and outside self-organized QDs (see Ref. [92] and the references therein). A variety of approaches are used to calculate such strain based on the numerical finite element method [93], molecular dynamics [94], and the valence force field [95], as well as the Green's function formalism [96] and the analogy between electrostatic problems and elasticity theory [97].

Calculation of elastic strain in crystalline systems with QDs encounters difficulties and rarely permits an analytic solution. On the other hand, investigations of QD systems by high-resolution X-ray diffractometry require the development of models taking the elastic strain distribution into account. This problem is further complicated by the necessity to calculate not only the elastic strain itself but also diffuse X-ray scattering from crystal lattice distortions caused by this strain. These difficulties may account for the small number of publications on the subject [69–72].

The theory of diffuse scattering is fairly well worked out for the spherically symmetric inclusion model [44, 50], but such QD self-organization occurs very rarely. As a rule, the QD size in the lateral direction is much bigger than its vertical size. The authors of Refs [69–72] considered cylindrical QDs with special reference to their elastic strain and stress relaxation on a free surface. In these reports, the solution for the calculation of diffuse scattering was represented as the product of the Fourier transform of the point defect displacement field and the QD shape function. Such an approach is not quite correct, in view of the difference between spatial variations of strain due to spheroidal and cylindrical inclusions [98]. On the other hand, this difference is not so important for the transformation of a spherically symmetric structure into a spheroidal one.

4.1 Diffuse scattering from epitaxial structures with quantum dots of different shapes

As was noted in the preceding section, of all the structural characteristics of nano-scale materials, the shape of the QDs and their elastic strain caused by the mismatch between QD lattice parameters and the matrix material play the most important role. The Stranski–Kastanow growth mode is known to lead to QD self-organization, the form of which strongly depends on the growth temperature, the relation between component flows, and the growth rate. Under certain conditions, QDs have the form of a lens, ellipsoid, dome, regular pyramid, or regular truncated pyramid with a square base (see Ref. [99] and the references therein).

The shape and size of QDs are studied by transmission electron and atomic force microscopy [99]. In recent years, scanning tunneling microscopy has found an increasingly frequent application in high-resolution structural studies [99]. As a rule, these methods allow the investigation of very small samples and mostly produce images of individual QDs. Moreover, cleavage leads to the destruction of the study objects. Hence the necessity of nondestructive techniques enabling the study of intact objects and providing information on the statistically averaged characteristics of semiconducting systems with QDs.

Following Ref. [52], we analyze diffuse scattering in a crystalline layer with buried QDs, regardless of their spatial correlation. The consideration of thin layers with nanoinclusions allows markedly simplifying general equations (3)–(6). As mentioned in Section 2.2, the scattering intensity angular distribution depends on the vector $\mathbf{q}$ determining the deviation of the diffraction vector from the RL node. The expression for the diffuse scattering intensity has the form

$$I_h^{\mathrm{d}}(\mathbf{q}) = K_{\mathrm{D}}\,\mathrm{Re}\left[\tau(\mathbf{q})\right], \tag{7}$$

where

$$\tau(\mathbf{q}) = \int_{-\infty}^{+\infty} \mathrm{d}\boldsymbol{\rho}\, g(\boldsymbol{\rho}) \exp\left(\mathrm{i}\mathbf{q}\boldsymbol{\rho}\right) \tag{8}$$

is the intrinsic correlation volume and K_{D} is a constant coefficient [50]. We recall that the term *correlation volume* was introduced in [38] by analogy with correlation length. With the strain fields outside QDs disregarded, the intrinsic correlation function $g(\boldsymbol{\rho})$ in (8) describes the shape of the QDs. At a reciprocal lattice node, with $\mathbf{q} = 0$, the correlation volume is equal to the QD volume V_{QD}:

$$\tau(0) = \int_{V_{\mathrm{QD}}} \mathrm{d}\boldsymbol{\rho}\, g(\boldsymbol{\rho}) = V_{\mathrm{QD}}\,.$$

The QD intrinsic correlation function in a crystalline matrix can be represented in the form of a convolution [49, 50]:

$$g(\boldsymbol{\rho}) = \frac{1}{V_{\mathrm{QD}}} \int D(\mathbf{r})\, D^*(\mathbf{r}+\boldsymbol{\rho})\, \mathrm{d}\mathbf{r}\,, \tag{9}$$

where the function $D(\mathbf{r})$ depends on the elastic strain field and describes local distortions in the crystal lattice. Substituting (9) in expression for correlation volume (8) yields

$$\tau(\mathbf{q}) = \frac{\left|D(\mathbf{q})\right|^2}{V_{\mathrm{QD}}}\,, \tag{10}$$

where $D(\mathbf{q})$ is the Fourier transform of $D(\mathbf{r})$.

Following [96], we consider the model of a medium with QDs periodically arrayed in three directions. In this case, the QD array strain tensor e_{rr} can be represented as a three-dimensional Fourier series:

$$e_{rr}(\mathbf{r}) = \frac{1}{V_L} \sum_{n_1,n_2,n_3} \tilde{e}_{rr}^{\mathrm{s}}(\boldsymbol{\xi}_n) \exp\left(\mathrm{i}\boldsymbol{\xi}_n\mathbf{r}\right), \tag{11}$$

where $V_L = d_1 d_2 d_3$, d_1, d_2, and d_3 are QD translational periods in the respective directions of the crystal with a cubic unit cell, and

$$\tilde{e}_{rr}^{\mathrm{s}}(\boldsymbol{\xi}) = \varepsilon_0 \tilde{\chi}_{\mathrm{QD}}(\boldsymbol{\xi}) \times \left[1 - \frac{C_{11} + 2C_{12}(C_{44}\xi^2/\xi_r^2 + C_{\mathrm{an}})^{-1}}{1 + (C_{12}+C_{44})\sum_{p=1}^{3} \xi_p^2/(C_{44}\xi^2 + C_{\mathrm{an}}\xi_p^2)}\right] \tag{12}$$

is the Fourier transform of the strain tensor component of an individual QD inside the cubic crystal [96]. Here, C_{11}, C_{12}, and C_{44} are elastic constants, the coefficient

$C_{an} = C_{11} - C_{12} - 2C_{44}$ describes the anisotropic part of the strain tensor, $\varepsilon_0 = (a_M - a_{QD})/a_M$ is the lattice mismatch strain, and a_M and a_{QD} are the constants of the basic matrix lattice and QDs.

Equation (12) involves the Fourier transform of the QD characteristic function $\chi_{QD}(\mathbf{r})$ [96],

$$\tilde{\chi}_{QD}(\xi) = \int_{V_{QD}} \chi_{QD}(\mathbf{r}) \exp(i\xi\mathbf{r})\, d\mathbf{r}, \tag{13}$$

where

$$\chi_{QD}(\mathbf{r}) = \begin{cases} 1, & \mathbf{r} \in V_{QD}, \\ 0, & \mathbf{r} \notin V_{QD}, \end{cases}$$

and integration is performed over the entire QD volume. We note that the QD characteristic function $\chi_{QD}(\mathbf{r})$ is an analog of the shape function in the X-ray diffraction theory and its Fourier transform $\tilde{\chi}_{QD}(\xi)$ structurally coincides with the correlation volume in the absence of elastic strain fields around QDs.

The projection of the elastic displacement field onto a distinguished direction is a result of integration of the strain tensor

$$U_r(\mathbf{r}) = \int_{\notin V_{QD}}^{r} e_{rr}(\mathbf{r}')\, d\mathbf{r}' + U_{r0}, \tag{14}$$

where U_{r0} is the initial displacement at the interface between a QD and the basic matrix. We recall that we do not take real mutual diffusion of matrix components and QDs into consideration. Substituting (11) in (14) finally leads to

$$U_r(\mathbf{r}) = \frac{1}{V_L} \sum_{n_1,n_2,n_3} \tilde{e}^{s}_{rr}(\xi_n) \frac{\exp(i\xi_n\mathbf{r})}{(\xi_n)_r} + U_{r0}, \tag{15}$$

where $\tilde{e}^{s}_{rr}(\xi_n)$ is given by (12).

The diffuse scattering amplitude in (10) can be represented as the sum of two terms,

$$D(\mathbf{q}) = D_{SW}(\mathbf{q}) + D_D(\mathbf{q}), \tag{16}$$

where the first term $D_{SW}(\mathbf{q})$ is the amplitude of diffuse scattering by the crystalline matrix, regardless of the elastic strain outside QDs (Stokes–Wilson scattering). The second term $D_D(\mathbf{q})$ accounts for the influence of lattice displacement fields near QDs. This term in sum (16) can be represented as

$$D_D(\mathbf{q}) = \int_{\notin V_{QD}}^{\infty} \left[1 - \exp(i\mathbf{hU})\right] \exp(i\mathbf{qr})\, d\mathbf{r}. \tag{17}$$

The numerical calculation of diffuse scattering from a crystal with buried QDs including elastic lattice displacements (15) can be conveniently done in a generalized spherical coordinate system. As a result, we have the following expression for the second term in (16):

$$D_D(\mathbf{q}) = -2\pi \frac{\mathbf{hq}}{q} \int_0^{\pi} d\theta \, \sin\theta\cos\theta \times \int_{r_0(\theta)}^{\infty} dr\, r^2 U_r(r,\theta) \exp(iqr\cos\theta), \tag{18}$$

where $r_0(\theta)$ is the distance between the center and the boundary of QDs in the vertical diffraction plane.

The above approach was used to simulate the diffuse scattering intensity distribution from an array of buried InAs QDs of different shapes in a GaAs basic matrix. The choice of QDs in the form of a cylinder was determined by the fact that it was the first model used to analyze diffuse scattering from the Si/Ge SL in the framework of the concept of point defects in an isotropic semi-infinite continuum [69–72]. Models of conical and spheroidal QDs respectively describe real growing QDs in the form of a pyramid or an ellipsoid. Also, the model of spheroidal QDs fairly well approximates frequently occurring QDs in the form of a lens [100]. Special attention given in our research to the analysis of diffuse scattering from pyramidal QD systems is attributable to difficulties of calculations. Another important reason to consider the above QD models is the existence of an analytic solution for the Stokes–Wilson scattering.

Calculations of diffuse scattering were done for symmetric reflection of (004) CuK_α radiation. In all the figures showing RSMs of diffuse scattering, the ratio of intensities between neighboring contours is given in the logarithmic scale and equals 0.316. The height of all QD models, except pyramidal inclusions, is $h = 5$ nm and the lateral size is $2R = 20$ nm. For a QD model in the form of a truncated cone, the angle α between the height and the generatrix is 45°. Elastic displacement distribution maps are represented in a linear scale with the ratio of lattice displacements between neighboring lines being 0.6×10^{-3} nm. Due to the large mismatch between InAs and GaAs lattice parameters, the distribution of strain inside QDs and very weak diffuse scattering from its internal part were disregarded in the calculations.

The pyramidal QD dimensions were chosen based on calculations of diffuse scattering on systems with spheroidal nanostructures of the same volume (height $h = 5$ nm, diameter $2R = 20$ nm). The following parameters for the pyramidal model were chosen under the assumption of equal volumes of QDs in the form of a spheroid and a truncated pyramid: the height $h = 4.37$ nm, the length of the upper and lower base edges $A_1 = 7.47$ nm and $A_2 = 16.2$ nm, the angle $\alpha = 45°$ between the base and one of the pyramid faces.

Analytic expressions for the Stokes–Wilson scattering by a crystalline medium with cylindrical, conical, and spheroidal QDs have the respective forms

$$D^{cyl}_{SW}(\mathbf{q}) = 2\pi \frac{Rh}{q_0} J_1(q_0 R) \operatorname{sinc}\left(\frac{q_z h}{2}\right),$$

$$D^{con}_{SW}(\mathbf{q}) = 2\pi \int_0^h dz\, \frac{R^{con}_z}{q_0} J_1(q_0 R^{con}_z) \exp(iq_z z),$$

$$D^{ell}_{SW}(\mathbf{q}) = 2\pi \int_{-h/2}^{h/2} dz\, \frac{R^{ell}_z}{q_0} J_1(q_0 R^{ell}_z) \exp(iq_z z),$$

where $J_1(q_0 R)$ is the first-order Bessel function, $\operatorname{sinc} x = \sin x/x$, $R^{con}_z = R + z\tan\alpha$ and $R^{ell}_z = R[1 - z^2/(h/2)^2]^{1/2}$ are conical and spheroidal QD radii depending on the coordinate z, and $q_0 = (q_x^2 + q_y^2)^{1/2}$.

The analytic solution for Stokes–Wilson scattering in the form of a truncated pyramid is written as

$$D_{SW}(\mathbf{q}) = 2\pi \frac{H}{q_x q_y} \Big[\operatorname{sinc}(Hq_1)\exp\big(-i(R_1 - Hq_1)\big) + \operatorname{sinc}(Hq_2)\exp\big(i(R_1 - Hq_2)\big) - \operatorname{sinc}(Hq_3)\exp\big(i(R_2 - Hq_3)\big) - \operatorname{sinc}(Hq_4)\exp\big(-i(R_2 - Hq_4)\big)\Big],$$

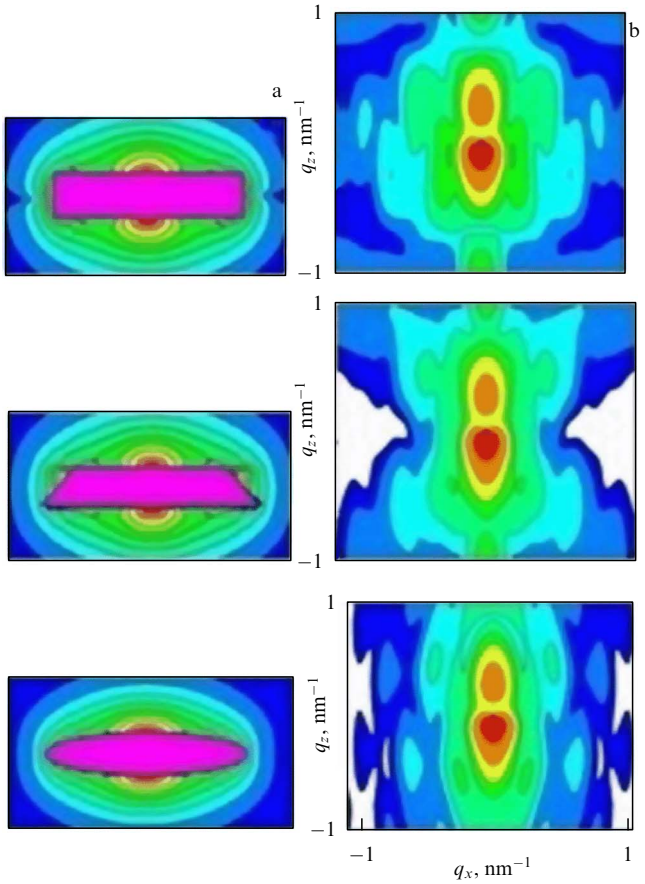

Figure 5. Two-dimensional maps of (a) the distribution of elastic displacement and (b) diffuse scattering from a CaAs crystalline matrix with InAs QDs in the form of a cylinder, truncated cone, and ellipsoid (from top down). The distance between adjacent QDs in the vertical and lateral directions is 500 nm [52].

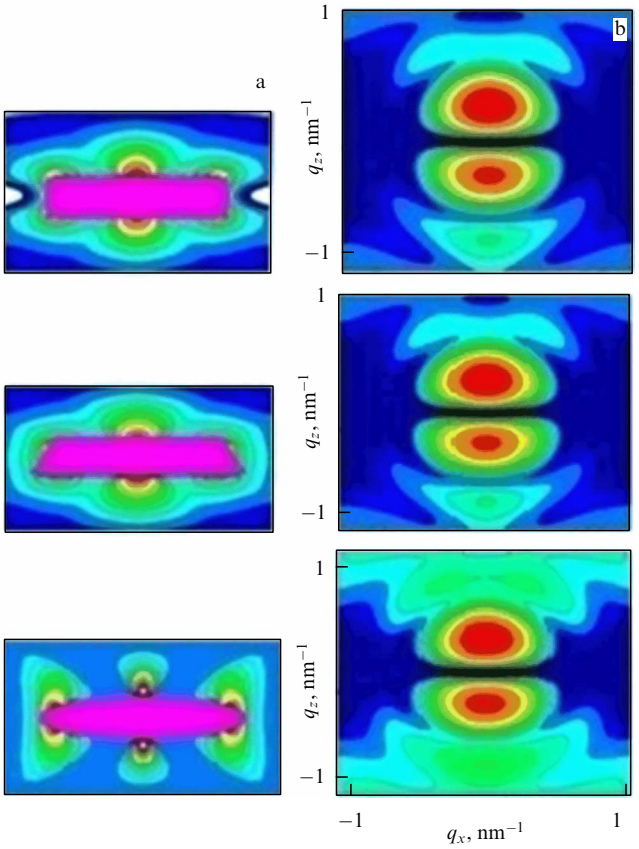

Figure 6. Two-dimensional maps of (a) the distribution of elastic displacement and (b) diffuse scattering from an InA/GaAs superlattice with uncorrelated InAs QDs in the form of a cylinder, truncated cone, and ellipsoid (from top down). The distance between adjacent QDs in the vertical direction is 30 nm [52].

with the angular parameters

$$q_1 = \frac{(q_x - q_y)\cot\alpha + q_z}{2}, \quad q_2 = \frac{(q_x - q_y)\cot\alpha - q_z}{2},$$

$$q_3 = \frac{(q_x + q_y)\cot\alpha + q_z}{2}, \quad q_4 = \frac{(q_x + q_y)\cot\alpha - q_z}{2},$$

and H being the pyramid height. The coefficients R_1 and R_2 have the form $R_{1,2} = (q_x A_1 \mp q_y A_2)/2$, where $A_{1,2}$ is the length of the upper and lower base edges.

Figure 5 presents elastic displacement and diffuse scattering maps in the case of a low QD packing density in the crystalline matrix. The mean distance between adjacent QDs is 500 nm. In this case, lattice displacement fields from QDs propagate over rather long distances. Such spatial changes in strain affect the angular distribution of diffuse scattering intensity. Lattice displacements near the center of a QD influence the formation of the diffuse scattering intensity distribution far from the RL node. For example, the contours of equal diffuse scattering by a crystal with conical QDs have a characteristic slope depending on the angle α between the cone height and the generatrix (see Fig. 5). Such intensity behavior near the RL node is also observed in the case of diffraction from crystalline islands with a trapezoidal cross section [101].

Figure 6 presents maps of the elastic displacement and diffuse X-ray scattering distribution for QDs with large packing density. The vertical distance between QDs is 20 nm. The distance between neighboring QDs in the lateral direction is 30 nm. Such a spatial arrangement of QDs is characteristic of nanostructured superlattices. In this case, elastic lattice displacement fields rapidly decay with distance. This means that the QD shape has only a weak effect on the diffuse scattering angular distribution (Fig. 6b). Therefore, the main factor in the analysis of diffuse scattering on superlattices with QDs is the ratio of the QD height to its lateral size, rather than the shape of nanoinclusions [102]. But the differences in the angular distribution of diffuse scattering from superlattices with QDs of different shapes do exist (Fig. 6b). They practically disappear if fluctuations of the QD size and spatial correlation are taken into account. Hence, analysis of diffuse scattering from superlattices with QDs by the HRXRD method can be done in the framework of a QD model that is the most convenient for numerical calculations. The model of choice for the purpose is that of ellipsoidal quantum dots.

We consider in more detail the results of numerical simulations of diffuse scattering from a crystalline medium with QDs in the form of a pyramid. The mismatch between the deformation of constant lattices of the GaAs matrix and InGaAs QDs is known to depend on the composition spatial distribution in the nanoinclusion boundary region. Two mismatch strain values $\varepsilon_0^{(1)} = 0.016$ and $\varepsilon_0^{(2)} = 0.003$ were used in numerical calculations.

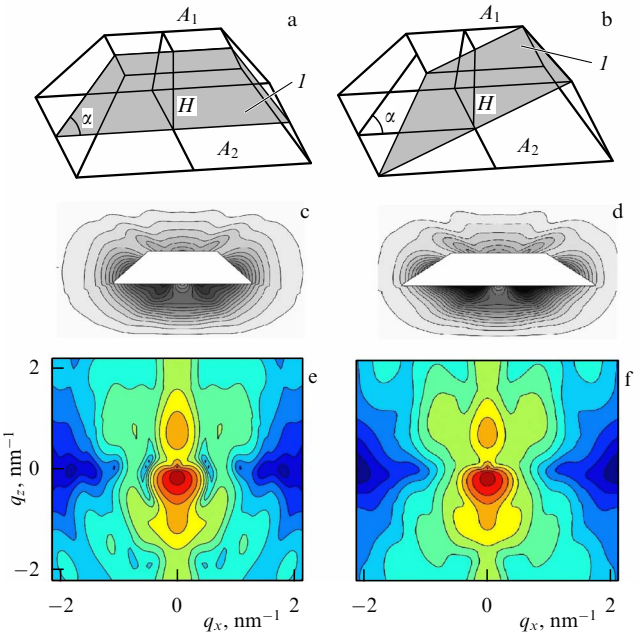

Figure 7. (Color online). (a, b) Orientation of the diffraction plane *1* (grey color) with respect to QD configuration; (c, d) respective 2D maps of elastic strains; and (e, f) diffuse scattering angular distribution. The distance between adjacent QDs in the vertical and lateral directions is 250 nm [52]; the mismatch strain is $\varepsilon_0^{(2)} = 0.003$ (c, d).

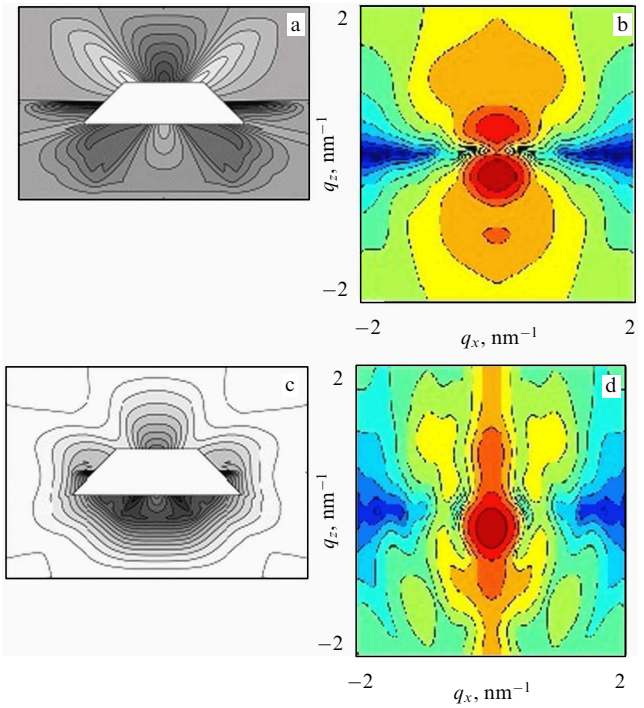

Figure 8. Two-dimensional maps of (a, c) elastic strains and (b, d) the angular distribution of diffuse scattering from an InAs/GaAs structure with uncorrelated InAs QDs in the form of a truncated pyramid for mismatch strains $\varepsilon_0^{(1)} = 0.016$ (a, b) and $\varepsilon_0^{(2)} = 0.003$ (c, d). The distance between adjacent QDs in the respective vertical and lateral directions is 20 and 30 nm.

We recall that the angular distribution of diffuse scattering from a crystal with pyramidal QDs depends on the nanostructure orientation with respect to the diffraction plane. Figure 7 shows two positions of the diffraction plane relative to the QD configuration for the azimuthal angles 0° (Fig. 7a) and 45° (Fig. 7b). Figures 7c, d present elastic displacement fields for a low QD packing density in the crystalline matrix. The mean distance between neighboring QDs is 250 nm in the vertical and lateral directions. The respective diffuse scattering distribution maps are depicted in Figs 7e, f.

Figure 8 presents two-dimensional elastic lattice displacement maps and the diffuse scattering angular distribution for QDs with a high packing density characteristic of superlattices in the absence of vertical and lateral correlation of nanostructures. The mean QD–QD distance is 20 nm, and the distance between neighboring QDs in the lateral direction is 30 nm. Numerical calculations demonstrate that the behavior of elastic strain and therefore the diffuse scattering angular distribution strongly depend on the mismatch strains between the QD lattice and crystalline matrix parameters.

For a relatively large strain ($\varepsilon_0^{(1)} = 0.016$), the contribution from Huang scattering becomes essential, as confirmed by the appearance of a 'zero line' at $q_z = 0$ on the diffuse scattering map (Fig. 8b). For a weak strain ($\varepsilon_0^{(2)} = 0.003$), the Stokes–Wilson scattering depending on the QD core shape prevails. In this case, the zero line is faint and the characteristic diffuse scattering behavior directly related to the slope of pyramidal QD faces becomes apparent (Fig. 8d). We recall that a similar characteristic slope of equal diffuse intensity contours was documented in a crystalline medium with conical QDs [52].

It follows from the foregoing that results of numerical calculations of the diffuse scattering angular distribution can be used for the nondestructive quantitative analysis of semiconducting systems with differently shaped QDs. The sole difficulty that remains to be overcome in self-organized QD growth technology is the production of equally sized nanostructures. For this reason, most RSMs show blurred scattering distribution contours, which means that a comparison with theoretical results in numerical calculations must take the QD size fluctuations into account.

4.2 Spheroidal quantum dots

High-resolution X-STM demonstrated that the shape of InAs QDs in a crystalline GaAs matrix is best described by an ellipsoid [6, 103, 104]. Moreover, it has recently been shown that InAsGaAs QDs coated with a thin $GaAs_{1-x}Sb_x$ layer also have an ellipsoidal shape [105]. Because the model of ellipsoidal (spheroidal) QDs markedly simplifies numerical computations, the detailed analysis below is limited to two independent approaches for the calculation of diffuse scattering from nanostructured systems in the framework of this model.

4.2.1 Analytic solution of the problem. We consider a crystalline medium with randomly distributed spheroidal QDs. The difference between the QD lattice parameter and the crystal lattice period of the basic matrix due to their different chemical compositions typically results in elastic mismatch strains on the inclusion boundary. The atomic displacement vector at a point **r** is written as

$$\mathbf{U}(\mathbf{r}) = \Lambda \int_V \frac{\mathbf{r} - \mathbf{r}'}{|\mathbf{r} - \mathbf{r}'|^3}\, \mathrm{d}\mathbf{r}',$$

where $\Lambda = \varepsilon_0(1+\nu)/(4\pi(1-\nu))$, $\varepsilon_0 = (a_{\rm in} - a_{\rm m})/a_{\rm m}$ is the mismatch between the inclusion lattice ($a_{\rm in}$) and the matrix ($a_{\rm m}$), ν is the Poisson coefficient, and V is the inclusion volume. The lattice displacement vector outside a QD is represented as a series $\mathbf{U}(\mathbf{r}) = \mathbf{U}_0(\mathbf{r}) + \mathbf{U}_1(\mathbf{r}) + \mathbf{U}_2(\mathbf{r}) + \ldots \mathbf{U}_n(\mathbf{r}) \ldots$, where each term has the form

$$\mathbf{U}_n(\mathbf{r}) = \Lambda(n+1)\,\frac{\mathbf{r}}{r^{n+3}}\,P_n(\cos\theta)\,\Omega_n\,. \tag{19}$$

Here, $\Omega_n = \int_V \mathrm{d}r'\,r'^n P_n(\cos\theta')$, $P_n(x)$ is the Legendre polynomial of degree n. Integration in the expression for Ω_n is over the QD volume.

We consider a spheroidal QD model [51]. Let l_z be the vertical elliptic axis and R the radius of a spheroid section in the lateral plane (lateral semi-axis). The radius $R_0(\theta) = R\{1 + [(R/(2l_z))^2 - 1]\cos^2\theta\}^{-1/2}$ describes the QD boundary. In this model, the coefficients Ω_n entering (19) can be written as

$$\begin{aligned}
\Omega_n &= \sum_{k=0}^{(n-1)/2} a_{nk} \int_{-1}^{1} \mathrm{d}x\,\frac{x^{2k-1}}{(1+cx^2)^{(n+3)/2}} \quad \text{for even } n\,,\\
\Omega_n &= \sum_{k=0}^{n/2} b_{nk} \int_{-1}^{1} \mathrm{d}x\,\frac{x^{2k}}{(1+cx^2)^{(n+3)/2}} \qquad \text{for odd } n\,,
\end{aligned} \tag{20}$$

where a_{nk} and b_{nk} are factors depending on the degree n of the Legendre polynomial and the term number k, and $c = (2R/l_z)^2 - 1$. It follows from relation (20) that only the coefficients Ω_n with even n have nonzero values. Substituting (20) in relation (19) after simple transformations shows that the lattice displacement vector $\mathbf{U}(\mathbf{r})$ outside the QD can be represented as the sum

$$\mathbf{U}(\mathbf{r}) = A\sum_{n=0}^{\infty} C_n \left(\left(\frac{l_z}{2}\right)^2 - R^2\right)^n P_{2n}(\cos\theta)\,\frac{\mathbf{r}}{r^{2n+3}}\,, \tag{21}$$

where $A = \Lambda V_{\rm ell}$, with $V_{\rm ell} = 2\pi l_z R^2/3$ being the QD volume. The coefficients C_n of the first 10 terms in sum (21) are

$$\begin{aligned}
&C_0 = 1\,,\ C_1 = 0.24\,,\ C_2 = 0.54\times10^{-1},\ C_3 = 0.12\times10^{-1},\\
&C_4 = 0.29\times10^{-2},\ C_5 = 0.67\times10^{-3},\ C_6 = 0.16\times10^{-3},\\
&C_7 = 0.37\times10^{-4},\ C_8 = 0.89\times10^{-5}, C_9 = 0.11\times10^{-6}\,.
\end{aligned}$$

The diffuse scattering amplitude in the formula for correlation volume (10) can be written as

$$D(\mathbf{q}) = D_{\rm SW}(\mathbf{q}) + D_{\rm H}(\mathbf{q}) + \sum_{n=1}^{\infty} D_n(\mathbf{q})\,, \tag{22}$$

where the first term $D_{\rm SW}(\mathbf{q})$ is the amplitude of diffuse scattering from the crystalline matrix without the elastic strain outside the QD. The second term in (22) describes Huang scattering by analogy with 'Coulomb' defects [43, 44]. This term, or the dipole term of the expansion, can be conveniently calculated in the generalized spherical coordinate system. This gives the expression for the Huang scattering amplitude

$$D_{\rm H}(\mathbf{q}) = \frac{2\pi A\mathbf{hq}}{q^2}\,\Phi_0(q, R, l_z)\,. \tag{23}$$

The function $\Phi_0(q, R, l_z)$ depends on $q = \sqrt{q_x^2 + q_y^2 + q_z^2}$ and the parameters R and l_z of the spheroid of interest:

$$\Phi_0(q, R, l_z) = \int_{-1}^{1} \mathrm{d}x\,\exp\left[\mathrm{i}q\rho(x, R, l_z)x\right],$$

where

$$\rho(x, R, l_z) = R\left\{1 + \left[\frac{R^2}{(l_z/2)^2} - 1\right]x^2\right\}^{-1/2}.$$

The multipole corrections to the diffuse scattering amplitude can be written, depending on the number n, in the form

$$D_n(\mathbf{q}) = 2\pi(-1)^{n+1}C_n A\left[\left(\frac{l_z}{2}\right)^2 - R^2\right]^n (\mathbf{hq})q^{2n-2}\Phi_n(q, R, l_z)\,,$$

where

$$\begin{aligned}
\Phi_n(q, R, l_z) = \int_{-1}^{1} \mathrm{d}x\,P_{2n}(x)x^{2n}\exp\left[\mathrm{i}q\rho(x, R, l_z)x\right]\\
\times f_n\left(\mathrm{i}q\rho(x, R, l_z)x\right).
\end{aligned}$$

The factor $f_n\left(\mathrm{i}q\rho(x, R, l_z)x\right)$ in the integrand is defined recursively,

$$f_n(r) = \frac{1}{2n-1}\left(\frac{1}{r^{2n-1}} + \frac{1}{2n-2}\left(\frac{1}{r^{2n-2}} + f_{n-1}(r)\right)\right),$$

with the initial value

$$f_1(r) = \frac{1}{r} + \frac{E_1(-r)}{\exp(r)}\,,$$

where

$$E_1(\mathrm{i}R) = \int_R^{\infty} \mathrm{d}z\,\frac{\exp(-\mathrm{i}z)}{z}$$

is the integral exponential.

Strictly speaking, the lattice displacement field $\mathbf{U}(\mathbf{r})$ of an individual QD in an unbounded crystalline medium tends to disappear as $\mathbf{r} \to \infty$. A different character of elastic strain relaxation is inherent in densely packed QDs in which the distances between nanostructures are comparable to their size. Therefore, the influence of neighboring QDs on the elastic displacement distribution can be taken into account by introducing the notion of the outer boundary of strain relaxation, i.e., the distances at which lattice displacement fields vanish. The solution of the boundary value problem leads to the conclusion that the factor $\mathbf{r}/r^{2n+3}$ in Eqn (21) should be substituted in each nth term of the multipole expansion by the expression

$$\left(1 - \frac{R_0^{2n+3}(\theta)}{R_1^{2n+3}}\right)^{-1}\left(\frac{1}{r^{2n+3}} - \frac{1}{R_1^{2n+3}}\right)\mathbf{r}\,,$$

where $R_0(\theta)$ is the distance determining the boundary of the QD surface and $R_1(\theta)$ is the distance from the center of the QD at which elastic displacement vanishes. As a result, lattice displacement vector (21) takes a more complicated

form:

$$\mathbf{U}^{\lim}(\mathbf{r}) = A\sum_{n=0}^{\infty} C_n\left(\left(\frac{l_z}{2}\right)^2 - R^2\right)^n P_{2n}(\cos\theta) \times \left(1 - \frac{R_0^{2n+3}(\theta)}{R_1^{2n+3}(\theta)}\right)^{-1}\left(1 - \frac{r^{2n+3}}{R_1^{2n+3}(\theta)}\right)\frac{\mathbf{r}}{r^{2n+3}}\,. \quad (24)$$

As $R_1(\theta) \to \infty$, expression (24) passes into (21).

To describe the boundary between neighboring QDs where elastic strain fields vanish, two geometric figures can be considered: a parallelepiped with sides $2d_x$, $2d_y$, $2d_z$ and a spheroid with semi-axes d_x, d_z (in our model, $d_x = d_y$). If the boundary has the form of a rectangular parallelepiped, the following expressions hold:

$$R_1(\theta) = \begin{cases} \dfrac{d_z}{2}\,, & \tan\theta = 0\,, \\ \dfrac{d_z}{2|\cos\theta|}\,, & \tan\theta \leqslant \dfrac{d_x}{d_z}\,, \\ \dfrac{d_x}{2|\sin\theta|}\,, & \tan\theta > \dfrac{d_x}{d_z}\,. \end{cases}$$

The spheroidal boundary is described by

$$R_1(\theta) = \frac{d_x}{2\sqrt{1 + \left((d_x/d_z)^2 - 1\right)\cos^2\theta}}\,.$$

Quantum dots, especially in the case of their high density in the growth plane, most frequently form a short-range order characteristic of lateral square lattices with the principal axes in the [100] and [010] directions. As mentioned above, square lattices have been produced from long-range-order nanostructures on specially prepared substrates with a periodic relief, referred to as quantum dot crystals [89–91]. Hence, when choosing the shape of the boundary of the elastic strain field where lattice displacements totally vanish, preference should be given to rectangular parallelepipeds. On the other hand, there are systems with QDs in which hexagonal lattices are formed from QDs [80]; in such cases, more sophisticated boundary conditions have to be introduced. In a certain approximation, the spheroid boundary model can be used to address the problem.

4.2.2 Numerical simulation. There are two methods for the study of X-ray diffuse scattering by a crystalline structure with spheroidal QDs in the framework of our analysis. One is the analytic solution of the problem, the other is the Green's function formalism. The next natural step is a comparative analysis of calculations of the scattering intensity angular distribution based on these two methods. For this, we consider a GaAs crystalline matrix in which spheroidal InAs QDs of the height $l_z = 5$ nm and lateral radius $R = 10$ nm are distributed. Results of numerical calculations of diffuse scattering are presented in the form of reciprocal space maps; the ratio of intensities between the neighboring lines for all contours is 0.38.

We first consider the case where the lattice displacement fields in spheroidal QDs are described by formula (21) and decay infinitely. If a spheroidal QD transforms into a spherically symmetric structure, the expression for elastic displacements in (21) retains only the zeroth term of the expansion described by the well-known 'Coulomb' strain relaxation with the distance from the QD boundary [44].

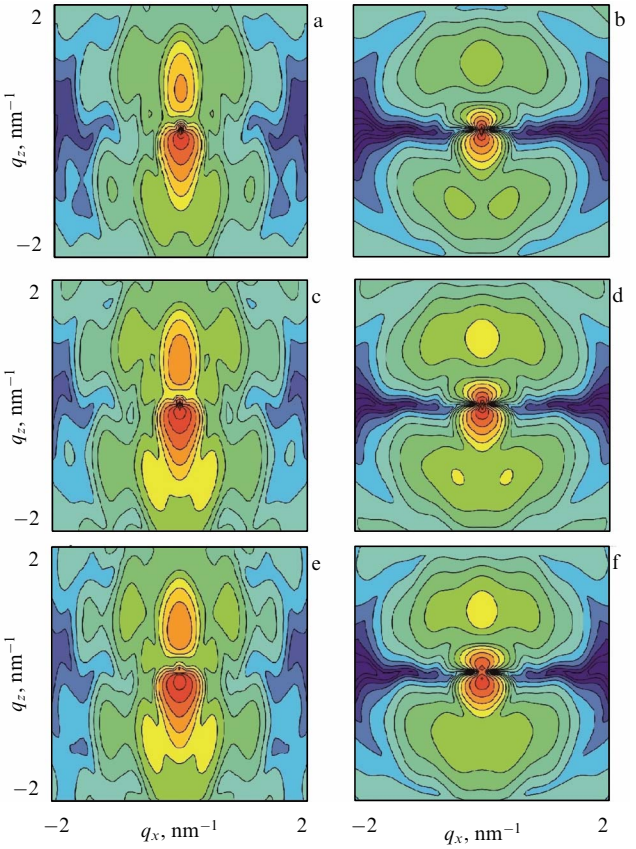

Figure 9. Simulated RSMs of diffuse scattering from a GaAs crystal with spheroidal QDs of low bulk concentration (QD–QD distance in vertical and lateral directions is 250 nm): (a–d) multipole expansion and (e, f) Green's function methods. (a, c, e) $\varepsilon_0^{(2)} = 0.003$, (b, d, f) $\varepsilon_0^{(1)} = 0.016$.

The more the $2R/l_z$ ratio differs from unity, the greater number of expansion terms must be taken into account in the numerical calculation of the scattering intensity. Simulations showed that seven terms of the multipole expansion are sufficient for calculations with the aforementioned QD dimensions ($2R/l_z = 4$). Considering the next terms introduces no further changes in the results of calculations within the computational error.

Figure 9 shows intensity distribution maps of diffuse scattering from a GaAs crystal with spheroidal InGaAs QDs for the mismatch strains $\varepsilon_0^{(2)} = 0.003$ (Fig. 9a, c, e) and $\varepsilon_0^{(1)} = 0.016$ (Fig. 9b, d, f). The maps are calculated by multipole expansion and Green's function methods. The top panel (Fig. 9a, b) corresponds to the QD model in which the elastic fields of lattice displacements do not intersect each other and vanish at infinity. Such a model can be realized only in the case of a very low concentration of QDs, the distance between which in three directions is much greater than 250 nm. For comparison, Figs 9c, d present the results of multipole calculations of diffuse scattering with the introduction of parallel planar boundaries between QDs at a distance of 125 nm from the center of the nanostructure. Although images of equal-intense contours are generally similar at first sight, they differ in the details.

Moreover, the contribution from Huang scattering becomes essential for a relatively large strain mismatch between the QD lattice and basic matrix parameters, as is evidenced by the appearance of the zero line at $q_z = 0$ on

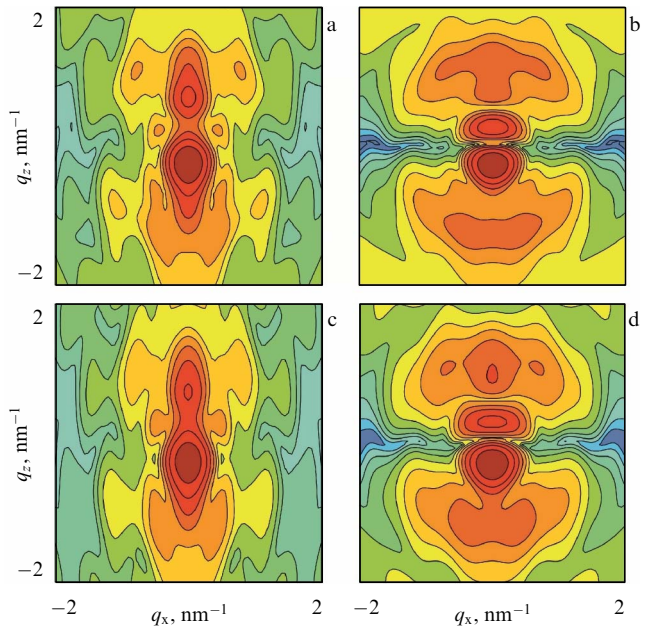

Figure 10. Simulated RSMs of diffuse scattering from a GaAs crystal with spheroidal QDs of high bulk concentration (the QD–QD distance in the respective vertical and lateral directions 20 and 30 nm): (a, b) multipole expansion and (c, d) Green's function methods. (a, c) $\varepsilon_0^{(2)} = 0.003$, (b, d) $\varepsilon_0^{(1)} = 0.016$.

the reciprocal space map (Fig. 9b, d, f). Stokes–Wilson scattering depending of the QD shape prevails for weak strain ($\varepsilon_0^{(2)} = 0.003$), when the trace of the zero line disappears (Fig. 9a, c, e). The Green's function method a priori implies a finite distance between adjacent QDs. Calculations of the diffuse scattering distribution maps with identical boundary conditions in the framework of the two independent approaches yield similar results (Fig. 9c, e and Fig. 9d, f), with minor differences for mismatch strains $\varepsilon_0^{(2)} = 0.003$ in the case of positive q_z values (Fig. 9c, e) and $\varepsilon_0^{(1)} = 0.016$ in the case of negative q_z (Fig. 9d, f).

Modern technology allows creating systems with QD arrays in which distances between neighboring nanostructures are comparable to their size. Such structures have a high density of self-organized nanostructures and elastic strain fields from QDs rapidly decreasing toward the boundaries with the nearest neighbors. Figure 10 presents intensity distribution maps of diffuse scattering from a GaAs crystal with spheroidal InGaAs QDs for the mismatch strains $\varepsilon_0^{(2)} = 0.003$ (Fig. 10a, c) and $\varepsilon_0^{(1)} = 0.016$ (Fig. 10b, d), calculated by the multipole expansion method (Fig. 10a, b) and using the Green's function (Fig. 10c, d). The distance between adjacent QDs in the vertical and lateral directions is 20 nm and 30 nm [106]. The QD–QD boundary is chosen in the form of a rectangular parallelepiped. The results of diffuse scattering calculations by two independent methods differ insignificantly, as in the case of a low concentration of nanostructures. On the whole, high QD concentrations are associated with broad scattering peaks and a slower decrease in intensity with the distance from the RL node. This suggests that the influence of Stokes–Wilson scattering in this event is greater than in the case of a low QD concentration.

Finally, numerical simulation has demonstrated that the form of the boundary conditions for the elastic strain field in the case of QDs spaced far apart from each other has practically no effect on diffuse scattering. In closely packed QDs, the equally intense contours for the boundaries in the form of a rectangular parallelepiped or a spheroid are significantly different. Moreover, the two approaches reveal a difference in the diffuse scattering angular distribution in the case of a spheroidal boundary. It is especially noticeable far from the RL node.

5. Spatial correlations in the arrangement of quantum dots

The ordering of QDs in a crystalline matrix of semiconducting structures (in other words, their spatial correlation) plays an important role in the tunneling of charge carriers in a quantum medium. Systems with vertically coupled QDs can serve as basic elements for injection heterolasers, solar cells, transistors, quantum computers, and other devices [1].

We recall that the QD spatial correlation can be described by long- and short-range order models. In the former case, the equilibrium positions of all QDs are fixed and have a strictly translational order. In the latter case, QDs obey the nearest-neighbor distribution law, but the strict periodic arrangement of all neighbors is absent. The nearest-neighbor distribution law can be used to derive the total distribution function. The short-range order can be described by introducing the radial distribution function [107] or based on the paracrystalline model described in Ref. [108].

QD arrays of various orderings are formed in semiconducting systems, depending on the growth conditions, including randomly distributed nanostructures, on the one hand, and regular structures (crystals) of QDs on the other hand. Evidently, there are no natural systems with strong translational ordering. Perfect crystals grown by modern technologies contain structural defects even at a first sight. This observation is true of nanostructured media formed, for example, by the lithographic technique or under conditions facilitating self-organization. Therefore, analyses of X-ray diffraction data must always include both coherent scattering from ordered objects and diffuse scattering in the case of random deviations from the statistically averaged ordering in the system.

A variety of deviations from the ordered spatial arrangement of nanostructures always occur in crystalline systems with QDs. Each deviation characteristically affects the scattering intensity angular distribution. We analyze the scattering intensity distribution in a reciprocal space in general terms using a superlattice with QDs as an example. Figure 11 schematically depicts the QD spatial correlation in a superlattice and illustrates its effect on the scattering intensity angular distribution.

We first consider X-ray diffraction from an ideal superlattice in the absence of QDs. Because there are neither random inhomogeneities nor other crystal lattice defects in the bulk superlattice, only coherent scattering is observed. Scattering intensity is distributed along the crystal truncation rod (CTR) (Fig. 11a). The intensity profile is a totality of vertical diffraction orders located at an angular distance inversely proportional to the superlattice period. If the superlattice contains a 3D periodic QD array that gives rise to an 'ideal crystal' of QDs, additional satellite maxima, besides CTRs, are formed near the RL node (Fig. 11b). The angular distance between satellites is inversely proportional to translational periods of QD nodes. In this case, coherent diffraction scattering occurs.

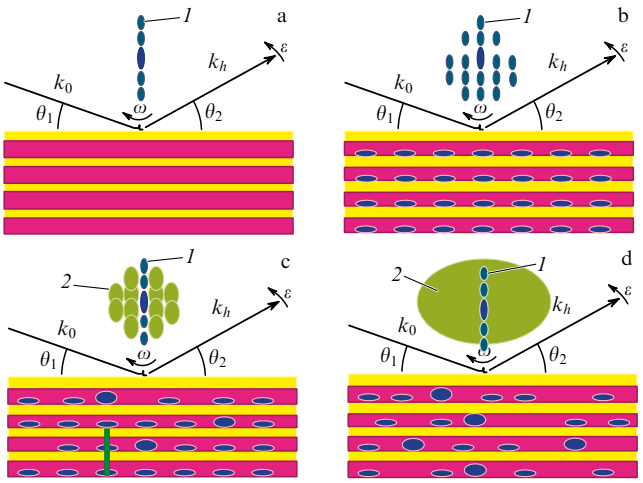

Figure 11. (Color online). Schematic of spatial correlation of QDs in a superlattice and its effect on the scattering intensity angular distribution. Blue color (areas *1*) depicts the intensity of coherent scattering, green color (areas *2*) is the intensity of diffuse scattering.

We assume that the 'crystal' made of QDs is not ideal. Then two cases are possible. In one of them, QDs randomly deviate from the nodes of the 3D lattice by a small distance without the loss of the average long-range order in their arrangement. This situation resembles a snapshot of thermal atomic oscillations in crystal lattice nodes. As a result, diffraction peaks retain their angular positions, and diffuse scattering maxima are formed around them (see Fig. 4). If distortions in the 3D lattice made of QDs do not preserve the long-range order, the additional diffraction satellites result from diffuse but not coherent scattering (Fig. 11c). Finally, if the QDs are arranged randomly, a blurred contour of diffuse scattering, characteristic of noncorrelated QDs of a certain shape, forms around a coherent CTR (Fig. 11d). X-ray diffraction in a semiconductor superlattice with chaotically distributed inclusions was theoretically investigated in Ref. [109]. The influence of the spatial correlation of defects on the formation of diffuse maxima was shown in Ref. [110].

Self-organized QDs in a superlattice typically retain the long-range order related to the superlattice period. But the stacking length is not preserved [111]; in other words, the vertical rows contain different numbers of QDs (Fig. 12). Moreover, the size of the QDs fluctuates, and the positions of their centers along the stacking line vary.

In the lateral direction, self-organized QDs preserve only the short-range order in their arrangement in superlattice layers. This shows that a thorough analysis of the influence of the spatial correlation of QDs on the scattering intensity angular distribution is needed.

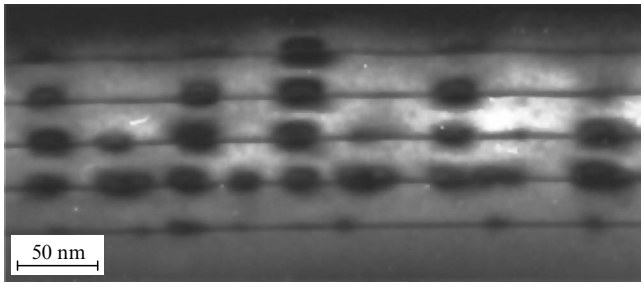

Figure 12. An InAs/GaAs quantum dot image obtained by TEM [111].

5.1 Lateral correlation of quantum dots. Short-range order

Following Ref. [112], we consider the influence of short-range order in the QD lateral arrangement on diffuse X-ray scattering. It is known that both paracrystalline and radial distribution models are based on the introduction of the probability function for the QD location, but the latter model is applicable only in the case of an isotropic QD distribution along the growth surface. We note that variants of the paracrystalline model were used to analyze experimental data by the GISAXS method [113, 114], triple-crystal X-ray diffractometry [114], and the GIXD technique [115]. The influence of the spatial QD correlation on diffuse scattering was theoretically considered with the use of the radial scattering function in Ref. [116].

The concept of an ideal paracrystalline lattice for point-like units [117] was used in [112] to develop a statistical theory of kinematic diffraction on epitaxial layers with QDs differing in the degree of lateral ordering.

QDs created by a self-assembly process in a crystalline layer under certain growth conditions destroy the translational order in the lattice and induce diffuse scattering. If the arrangement of QDs is spatially correlated, the expression for the diffuse scattering intensity should be written in the form

$$I_h^{\mathrm{d}}(\mathbf{q}) = K_{\mathrm{D}}\,\mathrm{Re}\left(T(\mathbf{q})\right). \tag{25}$$

Here, in contrast to (7), the intrinsic correlation volume $\tau(\mathbf{q})$ is substituted by another function $T(\mathbf{q})$ that takes the QD spatial correlation into account. In the absence of spatial correlation, the intrinsic correlation volume $\tau(\mathbf{q})$ is the Fourier transform of the Kato intrinsic correlation function $g(\boldsymbol{\rho})$. This function corresponds to the QD size and shape and the induced elastic strain near the QD. Because the diffuse scattering angular distribution depends not only on QD characteristics but also on their mutual spatial arrangement, we introduce the correlation function $G(\boldsymbol{\rho})$ taking both these factors into account. Such a function can be represented as a convolution of the QD spatial distribution function $W(\boldsymbol{\rho})$ and the QD intrinsic correlation function $g(\boldsymbol{\rho})$:

$$G(\boldsymbol{\rho}) = \int_{-\infty}^{\infty} \mathrm{d}\boldsymbol{\rho}'\, W(\boldsymbol{\rho}')\, g(\boldsymbol{\rho}' - \boldsymbol{\rho}). \tag{26}$$

We define the parameter of the angular distribution of diffuse scattering on spatially correlated QDs as the Fourier transform of $G(\boldsymbol{\rho})$,

$$T(\mathbf{q}) = \frac{1}{(2\pi)^2} \int_{-\infty}^{+\infty} \mathrm{d}\boldsymbol{\rho}\, G(\boldsymbol{\rho}) \exp\left(\mathrm{i}\mathbf{q}\boldsymbol{\rho}\right). \tag{27}$$

If QDs are distributed randomly, i.e., in the absence of any order in their arrangement, the correlation function $G(\boldsymbol{\rho})$ can be readily transformed into the intrinsic correlation function $g(\boldsymbol{\rho})$. With (26), correlation parameter (27) can be written as the product

$$T(\mathbf{q}) = \tau(\mathbf{q})\, F(\mathbf{q}), \tag{28}$$

where $\tau(\mathbf{q})$ is the correlation volume (shape function) of an individual QD and

$$F(\mathbf{q}) = \int_{-\infty}^{\infty} \mathrm{d}\boldsymbol{\rho} \exp(\mathrm{i}\mathbf{q}\boldsymbol{\rho})\, W(\boldsymbol{\rho}) \tag{29}$$

is the interference structural factor depending on the QD spatial ordering.

We consider a two-dimensional function $W(\rho_x, \rho_y)$ describing the short-range structural order in the arrangement of QDs. In this case, the equilibrium positions of all QDs are not fixed rigidly as was the case for the long-range order (see above). We choose two characteristic directions of QD arrangement in the lateral plane (x, y) given by basic vectors **a** and **b**. Let the nearest-neighbor position functions $H_1^{a,b}(\rho_x, \rho_y)$ be given, with superscripts a and b indicating the respective lateral directions. The degree of fuzziness of this function corresponds to the lateral disorder of QDs. The distribution of the second-nearest neighbors is given by the function

$$\begin{aligned} H_2^{a,b}(\rho_x, \rho_y) &= H_1^{a,b}(\rho_x, \rho_y) \otimes H_1^{a,b}(\rho_x, \rho_y) \\ &= H_1^{a,b}(\rho_x, \rho_y)^{\otimes 2}, \end{aligned}$$

where the symbol $\otimes$ denotes the convolution of functions. The convolution of a function with itself (autocorrelation) results in additional fuzziness, such that the resulting fuzziness increases, while the peak height decreases. Generalizing this reasoning to the description of the distribution of the next neighbors, e.g., those with a number m in the lateral direction **a**, we obtain

$$H_m^a(\rho_x, \rho_y) = H_1^a(\rho_x, \rho_y)^{\otimes m}. \tag{30}$$

It can be shown that the variance (mean square deviation) of the QD spatial distribution increases with m as $\Delta_m^a = \Delta_1^a \sqrt{m}$. Let the numbers of QDs in the directions of **a** and **b** equal N_a and N_b. If the number of QDs is finite, the functions $H_m^{a,b}(\rho_x, \rho_y)$ must be normalized to $(N_{a,b} - |m|)$, because the peak weight $W(\rho_x, \rho_y)$ decreases with increasing $|m|$. Therefore, for direction **a**, for example, we must write

$$\begin{aligned} W^a(\rho_x, \rho_y) &= \delta(\rho_x) \\ &+ \sum_{m=1}^{N_a} \frac{N_a - |m|}{N_a} \left(H_m^a(\rho_x, \rho_y) + H_{-m}^a(\rho_x, \rho_y) \right). \end{aligned} \tag{31}$$

The other dependence, $W^b(\rho_x, \rho_y)$, can be written similarly; hence, the lateral QD distribution is described by a convolution of these functions. As a result, we obtain the interference structural factor

$$F(q_x, q_y) = F_a(q_x, q_y)\, F_b(q_x, q_y), \tag{32}$$

where structural factors of different directions are

$$\begin{aligned} F_{a,b}(q_x, q_y) &= 1 + \frac{2}{N_{a,b}} \\ &\times \mathrm{Re} \left\{ \frac{Z_1^{a,b}(q_x, q_y) \left[\left(1 - Z_1^{a,b}(q_x, q_y)\right) N_{a,b} - \left(1 - Z_1^{a,b}(q_x, q_y)^{N_{a,b}}\right) \right]}{\left(1 - Z_1^{a,b}(q_x, q_y)\right)^2} \right\}. \end{aligned} \tag{33}$$

Here,

$$\begin{aligned} &Z_1^{a,b}(q_x, q_y) \\ &= \int_{-\infty}^{+\infty} \mathrm{d}\rho_x \int_{-\infty}^{+\infty} \mathrm{d}\rho_y \exp\left[\mathrm{i}(q_x \rho_x + q_y \rho_y)\right] H_1^a(\rho_x, \rho_y) \end{aligned} \tag{34}$$

are the Fourier transforms of the unit distribution functions of QDs.

We recall that a solution of type (33) for the model of scattering elements with a one-dimensional quasi-periodic lattice was obtained in the framework of a different theoretical approach [118]. In the case of an infinite number of QDs ($N_{a,b} \to \infty$), the interference structural factor in (33) is simplified [113–115]. In the traditional triple-crystal X-ray diffraction scheme, the scattering intensity angular distribution in the RS depends on the parameters q_x and q_z. Therefore, the expression

$$\bar{F}(q_x) = \int_{-\infty}^{\infty} \mathrm{d}q_y\, F(q_x, q_y) \tag{35}$$

should be used instead of (33) for numerical calculations in the framework of this scheme. The solutions thus obtained were used to numerically simulate the angular distribution of coherent and diffuse scattering from an InGaAs/GaAs(001) system with ellipsoidal InAs QDs. Calculations were done using parameters corresponding to (004) reflection of σ-polarized $\mathrm{CuK}_{\alpha 1}$ radiation. The QDs were 10 nm high and 20 nm in diameter. The spatially correlated QDs in the epitaxial InGaAs layer formed a random square lattice; its fuzziness was described by the normal (Gaussian) distribution. Calculations were done for a large number of QDs ($N_{a,b} \to \infty$). The QD distribution functions $W(\rho_x)$ for different dispersion values and the corresponding interference structural factors $\bar{F}(q_x)$ are presented in Fig. 13.

Calculated scattering intensity distribution maps near the (004) GaAs RL node are shown in Fig. 14. The vertical central strip corresponds to coherent scattering on the InGaAs layer with QDs and the semi-infinite GaAs substrate. In the absence of spatial correlation, equal-intensity contours are related to typical Huang scattering from a layer with randomly distributed QDs (Fig. 14a). Diffraction patterns are markedly altered in the case of a short-range order in the QD arrangement (Fig. 14b, c). Additional interference fringes characterizing the degree of QD lateral ordering appear (Fig. 14c). Fuzziness of the lateral lattice leads to a proportional widening of the interference fringes (Fig. 14b). We note that such characteristic interference fringes from spatially oriented SiGe islands were observed experimentally near the (004) Si node on the scattering intensity distribution maps [114].

5.2 Vertical correlation of quantum dots

The first model for the description of the vertical correlation of QDs in the X-ray diffraction theory was considered in Ref. [69]. In accordance with the formalism of the stationary random process theory [119], the authors introduced the correlation function governing the diffuse scattering behavior depending on the QD ordering. If the correlation length tended to infinity, diffuse scattering was determined by the superlattice structural factor. In another limit case, with the zero correlation length, the diffuse scattering intensity was proportional to the number of periods of the multilayer structure.

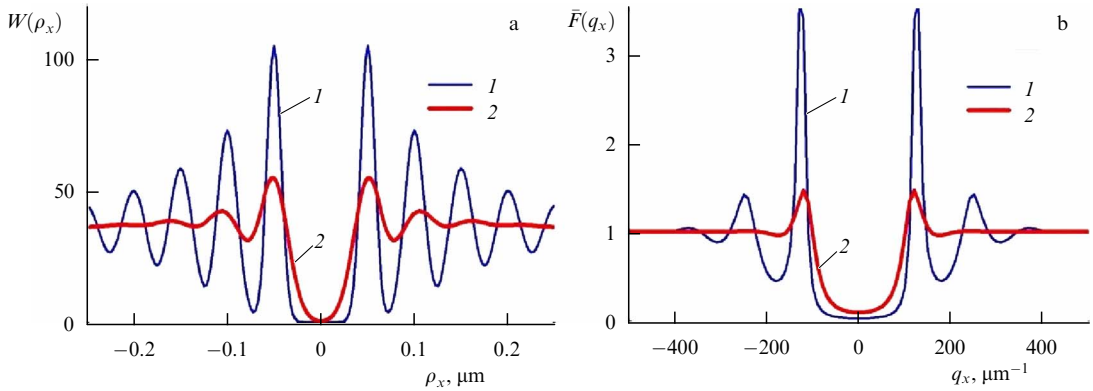

Figure 13. (a) QD distribution functions $W(\rho_x)$ (not taking the central δ-shaped maximum into account) and (b) the corresponding interference structural factors $\bar{F}(q_x)$. The mean distance between QDs is $T_a = 50$ nm, the variance $\Delta^a = 0.15T_a = 7.5$ nm (*1*), $\Delta^a = 0.3T_a = 15$ nm (*2*) [110].

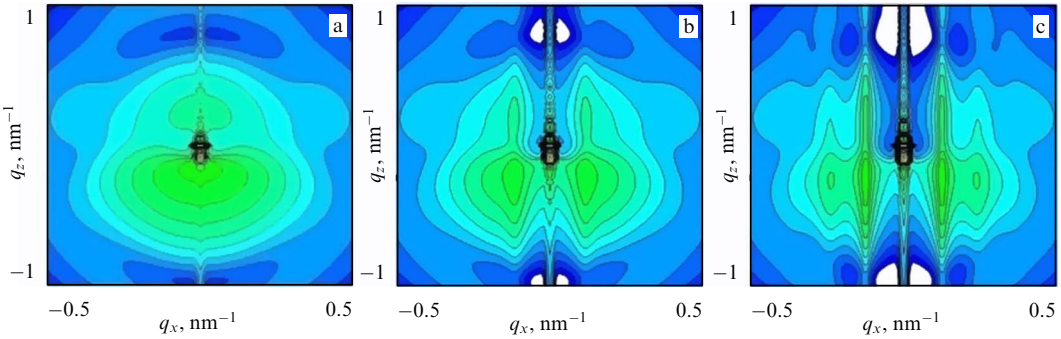

Figure 14. Simulated maps of the intensity distribution for scattering on the InGaAs/GaAs system with QDs near the (004)GaAs node of the reciprocal lattice (a) with and (b, c) without spatial correlation. The mean distance between QDs is $T_a = 50$ nm, the variance (b) $\Delta^a = 0.3T_a = 15$ nm, (c) $\Delta^a = 0.15T_a = 7.5$ nm. The ratio of intensities of neighboring contours presented on the logarithmic scale is 0.45.

A model of QD lateral deviations from the stacking midline was proposed in [120] based on the results of investigations of X-ray diffraction on a superlattice in the grazing geometry. In this model, the deviation variance increases with the superlattice period number n as $\sigma_n = \sqrt{n}\sigma$, where σ is the variance of the first (bottom) superlattice layer. Such behavior of the variance is characteristic of short-range structural order [114].

The above models ignore the principal feature of the growth structure of superlattices with QDs, i.e., the stacking length. Indeed, the number of vertically coupled QDs in the bulk of a multilayer structure is subject to variation (see Fig. 12), and the stacking length is not always equal to the thickness of a multilayer system. Moreover, the blurring of diffuse maxima depends on the mean stacking length rather than the QD lateral fluctuations in the lateral plane. Because the number of vertically coupled QDs is the main parameter measured by modern instruments of nano- and optoelectronics, we consider some details of the model taking the vertical QD correlation into account in a superlattice depending on the stacking length [121].

The arrangement of QDs in the vertical direction along the z axis is known to have a strict long-range order due to periodic alternations of layers differing in chemical composition. In the lateral direction, self-organized QDs usually create a short-range order that can be described by the paracrystalline model [112]. The QD spatial distribution function $W(\boldsymbol{\rho})$ can be written as the product

$$W(\boldsymbol{\rho}) = W_{\mathrm{L}}(\rho_x, \rho_y)\, W_{\mathrm{V}}(\rho_z)\,, \tag{36}$$

where $W_{\mathrm{L}}(\rho_x, \rho_y)$ and $W_{\mathrm{V}}(\rho_z)$ describe lateral and vertical spatial arrangements of QDs. The lateral QD distribution is not considered here because the detailed analysis of $W_{\mathrm{L}}(\rho_x, \rho_y)$ is presented in Section 5.1. We assume for simplicity that $W_{\mathrm{L}}(\rho_x, \rho_y) \equiv 1$.

We examine the correlation function $W_{\mathrm{V}}(\rho_z)$ in more detail. Let a function $w(z)$ define the probability for a nanoparticle to be at a point z; then the position of another particle at a point z' shifted strictly vertically by $\rho_z = z - z'$ is described by the function $w(z')$. The vertical correlation function can by definition be represented in the form of a convolution [122],

$$W_{\mathrm{V}}(\rho_z) = \int_{-\infty}^{+\infty} \mathrm{d}z\, w(z)\, w(z - \rho_z) = \int_{-\infty}^{+\infty} \mathrm{d}z'\, w(z')\, w(z' + \rho_z)\,. \tag{37}$$

The formation of vertically coupled QDs is usually determined by the conditions of the growth technology being used and depends on a variety of parameters, such as the elastic strain distribution, the thickness of wetting and spacing layers, their composition, the growth temperature, and so on. Sequential deposition of wetting and spacing layers gives rise to a superlattice with QD arrays characterized by translational ordering in the vertical direction. The translational period corresponds to the period of superlattice modulation of the composition. Therefore, the function $w(z)$ describing QD stacking is periodic, $w(z) = w(z + l_{\mathrm{SL}})$. Let l_{V} be the vertical distance (the superlattice thickness) over which QDs are arranged strictly above one another to form a

vertical column. This distance can be called the stacking thickness, while the distance l_V is referred to as the vertical correlation length.

It follows from the foregoing that correlation parameter (28) can be written as the product

$$T(\mathbf{q}) = \tau(\mathbf{q})\, F_V(q_z)\,. \tag{38}$$

The influence of coupled QDs on the diffuse scattering distribution is described by the interference structural factor

$$F_V(q_z) = \int_{-\infty}^{+\infty} \mathrm{d}\rho_z \, \exp\left(\mathrm{i}q_z\rho_z\right) W_V(\rho_z)\,. \tag{39}$$

Substituting (37) in expression (39) for the interference structural factor along the vertical direction z yields

$$F_V(q_z) = \left| \int_{-\infty}^{+\infty} \mathrm{d}z\, w(z) \exp\left(\mathrm{i}q_z z\right) \right|^2 . \tag{40}$$

The interference structural factor of stacked QDs is written as

$$F_V(q_z) = \begin{cases} F_V(q_z, l_V)\,, & |z| \leqslant l_V\,, \\ 1\,, & |z| > l_V\,, \end{cases} \tag{41}$$

where

$$F_V(q_z, l_V) = \left| \frac{1}{2l_V} \int_{-l_V}^{l_V} \mathrm{d}z\, w(z) \exp\left(\mathrm{i}q_z z\right) \right|^2 . \tag{42}$$

Such a representation of the stacked QD structural factor means that interference diffuse scattering in the vertical direction is produced by QDs periodically arranged along the z axis at the spacing given by the correlation length. Correlation effects are absent outside the stacking thickness; therefore, $F_V(q_z) \equiv 1$. If the superlattice contains no vertically aligned QDs, i.e., the correlation length l_V is smaller than the superlattice period l_{SL}, the interference factor in the vertical direction is always unity. This means that the intensity angular distribution profile contains no diffuse scattering superstructure orders (satellites). In this case, the shape of diffuse lines depends only on averaged structural characteristics of the QDs randomly distributed along the z axis and is described by their intrinsic correlation volume (8).

Because $w(z)$ is a periodic function, as was noted above, it can be regarded in the model of a long-range order and written as a Fourier series,

$$w(z) = \sum_{n=-\infty}^{\infty} B_n \exp\left(-\mathrm{i}nK_{SL}z\right), \tag{43}$$

where $K_{SL} = 2\pi/l_{SL}$ is the superlattice modulation period in reciprocal space (the distance between diffraction satellites). The Fourier coefficients in (43) are

$$B_n = \frac{1}{l_{SL}} \int_{-l_{SL}/2}^{l_{SL}/2} w(z) \exp\left(\mathrm{i}nK_{SL}z\right) \mathrm{d}z\,. \tag{44}$$

Substituting (43) in (42) yields

$$F_V(q_z, l_V) = \sum_{n=-\infty}^{\infty} \left| B_n \, \frac{\sin\left[\left(q_z - nK_{SL}\right) l_V\right]}{\left(q_z - nK_{SL}\right) l_V} \right|^2 . \tag{45}$$

The QD interference factor of stacked QDs in form (45) has a clear physical meaning. Superstructural maxima of diffuse scattering on the superlattice with vertically aligned QDs form near the RL node at $q_z^{SL} = nK_{SL} = 2\pi n/l_{SL}$, where $n = 0, \pm1, \pm2, \ldots$ is the number of the diffuse satellite. Diffuse intensity maxima are defined by the Fourier coefficients B_n. According to (44), their values depend on the statistical distribution of QD centers. Due to the difference in the QD size, these centers can shift with respect to the heteroboundary between wetting and spacing layers. The width of diffuse satellites in RSs in the vertical direction depends on the correlation length l_V. Because the width of the neighboring vertical columns of QDs in a superlattice with self-organized QDs can be different (see Fig. 12), the statistically averaged correlation length $\bar{l}_V$ and the corresponding variance of its probability distribution must be introduced to describe diffuse scattering. The interference factor of stacked QDs can then be written as

$$F_V(q_z, \bar{l}_V) = \sum_{n=-\infty}^{\infty} |B_n|^2 \, \Psi(q_z, \bar{l}_V, n)\,, \tag{46}$$

where $\Psi(q_z, \bar{l}_V, n)$ is determined by the probability function for the correlation length distribution $p(z, \bar{l}_V)$ over the superlattice thickness:

$$\Psi(q_z, \bar{l}_V, n) = \int_0^{\infty} \left| \frac{\sin\left[\left(q_z - nK_{SL}\right)z\right]}{\left(q_z - nK_{SL}\right)z} \right|^2 p(z, \bar{l}_V)\, \mathrm{d}z\,. \tag{47}$$

We consider the model where the vertical probabilistic function for the QD distribution in the interval $(-l_{SL}/2; l_{SL}/2)$ has the form

$$w(z) = \exp\left(-\frac{|z|}{a}\right). \tag{48}$$

Fourier coefficients (44) for this exponential have the analytic expression

$$B_n = \frac{2a/l_{SL}}{1 + 4\pi^2 (a/l_{SL})^2 n^2} \left[1 - \mathrm{i} \exp\left(-\frac{l_{SL}}{2a}\right)(-1)^n\right]. \tag{49}$$

Numerical simulation of the diffuse scattering angular distribution was performed for a 20-period InAs/GaAs superlattice with ellipsoidal QDs [51]. The superlattice period was 20 nm and the GaAs spacer thickness 15 nm. The mean lateral QD radius was $R = 12.5$ nm and the height $l_z = 5$ nm. Statistical averaging over the QD dimensions and the correlation length was done with the use of the log normal distribution. The variance of QDs spread over dimensions was 30% of the QD radius and height. Formula (48) describing the vertical QD distribution was used in the calculations, with the parameter $a = 3$ nm.

Figure 15a presents a map of the diffuse scattering angular distribution in the absence of vertical correlation. It applies under the condition $l_V < l_{SL}$; in other words, a multilayer structure does not contain stacked QD columns. Here and on the next maps, the equal-intensity contours of diffuse scattering are shown on a logarithmic scale. The ratio of intensities between adjacent lines is 0.4. The diffuse scattering pattern depicted in Fig. 15a is in excellent agreement with equal-intensity contours for a crystal with randomly arranged ellipsoidal inclusions, which means that incoherent scattering on the superlattice in the absence of vertical QD correlation is

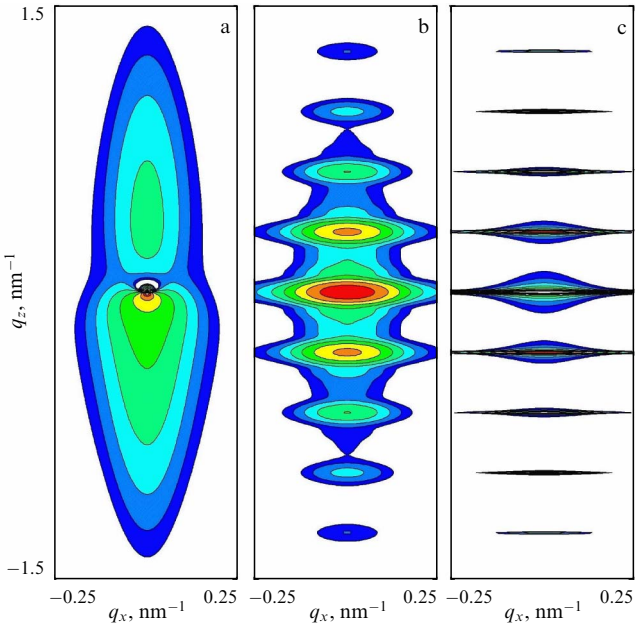

Figure 15. Simulated maps of the spatial distribution of X-ray radiation diffuse scattering by a 20-period superlattice with QDs: (a) in the absence of vertical correlation, $l_V < l_{SL}$; mean correlation length $\bar{l}_V = 2l_{SL}$ (b), $\bar{l}_V = 20l_{SL}$ (c); stacking variance $\sigma_V = \bar{l}_V/4$.

not accompanied by the formation of diffuse scattering superstructural satellites.

Figure 15b illustrates the effect of the correlation length (stacking thickness) on the formation of the diffuse scattering angular distribution. In the case of a short correlation length $\bar{l}_V = 2l_{SL}$, diffuse maxima satellites blur in the vertical direction (Fig. 15b), and the half-width of diffuse peaks is $\Delta q_z \approx 0.035$ nm. Figure 15c shows the formation of the diffuse scattering pattern under the condition $\bar{l}_V = 20l_{SL}$, i.e., the total vertical QD correlation. The angular intensity distribution for scattering on stacked QDs over the entire superlattice thickness is characterized by the appearance of relatively high and narrow ($\Delta q_z \approx 0.0035$ nm^{-1}) diffuse satellites.

6. Quantitative X-ray diffraction analysis of heterostructures with quantum dots

Electron microscopy and X-ray diffraction are mutually complementary methods used in research on semiconducting systems with QDs [123]. TEM provides information at the atomic level for samples of very small volumes, whereas X-ray diffractometry allows obtaining averaged characteristics of the entire object. Because the diffraction techniques are indirect, the main problem encountered in their application is the need to design a rather complicated procedure for the reconstruction of the intricate structure of the study material based on the scattering intensity angular distribution.

The first attempts to obtain information about crystalline systems with QDs by means of RSM analysis were undertaken in Refs [69, 70] using the Krivoglaz kinematical diffraction theory [44]. However, such an approach cannot be regarded as a quantitative analysis because it takes only diffuse scattering into account (Fig. 2a). As a rule, the intensity of diffuse scattering is lower than that of the coherent component, even though it is distributed within a broad RS angular interval. Diffuse and coherent scattering intensities overlap near the RL node and thereby give rise to the total reflected intensity contour, meaning that the qualitative analysis of crystalline media with QDs requires a number of sequential operations. First and foremost, coherent and diffuse scattering can be taken into consideration simultaneously by using the formalism of the Kato statistical diffusion theory [28]. A model of the medium has to be constructed based on a priori information about the growth structure.

It should be borne in mind that a model-independent solution of the inverse diffraction problem is impossible in this case, because rather intricate structures are investigated and both coherent and diffuse scattering channels have to be considered. Moreover, numerical calculations should include the statistical dispersion of QD dimensions. Experimental RSM of semiconducting systems with QDs are large data arrays to be processed in the general case with the use of modern supercomputers. Another approach to the solution of the problem is based on identifying vertical and horizontal RSM sections along coherent and diffuse maxima. Finally, the quantitative analysis is substantially simplified if experimental diffraction data are considered together with results obtained by other methods, e.g., TEM [123].

6.1 Short-period superlattices with quantum dots

Short-period superlattices with QDs, i.e., multilayer structures with ultrathin spacers, are presently the main focus of research [1]. Therefore, we first consider the application of high-resolution X-ray diffractometry to the nondestructive quantitative analysis of a periodic structure with vertically ordered QDs. The analysis is based on numerical simulation of the *total scattering intensity* maps $I_h^t(\mathbf{q}) = I_h^c(\mathbf{q}) + I_h^d(\mathbf{q})$ near a certain RL node, where $I_h^c(\mathbf{q}) \sim f^2$ and $I_h^d(\mathbf{q}) \sim (1 - f^2)$ are the respective intensities of coherent and diffuse scattering and f is the static Debye–Waller factor. It is known that coherent scattering data contain information about the thickness of the wetting layer and its mean concentration gradient, the spacer thickness, period fluctuations in QD superlattices, composition variations of the superlattice period, etc.

It was mentioned above that the statistical distribution of QDs in the plane of epitaxial layers allows regarding them as local structural defects responsible for diffuse scattering and attenuation of the coherent part of the total X-ray diffraction scattering. In general, the static Debye–Waller factor relating diffuse and coherent components is the product $f = f_{QD} f_s$, where $f_{QD} = \exp(-c_{QD} V_{QD})$ is the static factor caused by the presence of QDs without elastic strain and f_s is the static factor associated with elastic strain around QDs and other deviations from the translational order in the crystal lattice (point-like and extended defects, interface roughness, etc.). Here, c_{QD} is the bulk QD concentration and V_{QD} is the mean QD volume.

Unlike coherent scattering, the diffuse component contains information about QDs, including their size, shape, elastic strain, and lateral and vertical spatial correlation. Because we have already conducted a detailed study of the origin of diffuse scattering from a crystalline medium with QDs, we consider the analytic solution for X-ray coherent scattering in a multicomponent (polytypic) superlattice with QDs [124–126].

A characteristic parameter of such a superlattice is its period consisting of P layers with different lattice parameters.

Let d be the lattice spacing of the crystalline substrate, and d_p be the lattice spacings and l_p the thicknesses of individual layers of the period, where $p = 1, 2 \ldots P$ gives the layer number. Then the mean lattice spacing of a multicomponent superlattice is written as $d_{\rm SL} = \sum_{p=1}^{P} d_p l_p / l_{\rm SL}$, where $l_{\rm SL} = \sum_{p=1}^{P} l_p$ is the superlattice period thickness. The perfection of the crystal lattice in each superlattice layer is determined by the static Debye–Waller factor f_p.

The solution for the amplitude coefficient of coherent X-ray wave reflection from an N-period multicomponent superlattice is given by

$$R^{\rm c}_{\rm SL}(q_x, q_z) = {\rm i} F_{\rm c}(q_z)\, N_{\rm c}(q_z)\, W(q_x) \times \exp\left({\rm i}(N-1)\sum_{p=1}^{P} A_p(q_z)\, l_p\right), \qquad (50)$$

where

$$W(q_x) = \int_{-L_x/2}^{L_x/2} {\rm d}x\, \exp({\rm i} q_x x)$$

is the parameter depending on the X-ray beam size and L_x is the lateral size of the exposed superlattice surface. The Laue interference function of the multicomponent superlattice has the form

$$N^{\rm c}(q_z) = \frac{\sin\left(N\sum_{p=1}^{P} A_p(q_z)\, l_p\right)}{\sin\left(\sum_{p=1}^{P} A_p(q_z)\, l_p\right)},$$

were $A_p = (a_0^{(p)} - q_z + \varepsilon_p h)/2$ is the angular parameter and ε_p is the lattice strain in the pth layer of the superlattice period. The structural amplitude of a multicomponent superlattice is written as

$$F^{\rm c}_{\rm SL}(q_z) = \sum_{p=1}^{P} a_h^{(p)} f_p \frac{\sin\left(A_p(q_z)\, l_p\right)}{A_p(q_z)} \times \exp\left({\rm i}\sum_{k=1}^{p-1} 2A_k(q_z)\, l_k + {\rm i} A_p(q_z)\, l_p\right).$$

The coefficients $a_h^{(p)} = C\pi\chi_h^{(p)}/(\lambda\gamma_h)$ characterize interaction of the X-ray field with the medium electron density of alternating superlattice layers, where $\gamma_h = |\sin\theta_{\rm B}|$ and $\theta_{\rm B}$ is Bragg's angle, C is the polarization factor, and λ is the X-ray radiation wavelength in a vacuum. Fourier components of the X-ray polarizability $\chi_h^{(p)}$ are related to the superlattice layer structural factors $F_{hkl}^{(p)}$ as $\chi_h^{(p)} = -r_0\lambda^2 F_{hkl}^{(p)}/(\pi V_{\rm c})$, where $V_{\rm c}$ is the unit cell volume, $r_0 = e^2/(mc^2)$ is the classical electron radius, and e and m are the electron charge and mass. In the case of a two-component superlattice ($p = 1, 2$), solution (50) takes the form

$$R^{\rm c}_{\rm SL}(q_x, q_z) = {\rm i} F^{\rm c}_{\rm SL}(q_z) \exp({\rm i}\psi)\, \frac{\sin(Ny)}{\sin y}\, W(q_x), \qquad (51)$$

where $y = A_1 l_1 + A_2 l_2$, $A_{1,2} = (a_0 - q_z + \varepsilon_{1,2} h)/2$, and $\psi = (N-1)y + A_1 l_1$. The superlattice structural amplitude is written as

$$F^{\rm c}_{\rm SL}(q_z) = a_h^{(1)} f_1 \frac{\sin(A_1 l_1)}{A_1} + \exp({\rm i}y) a_h^{(2)} f_2 \frac{\sin(A_2 l_2)}{A_2}.$$

For complex multilayer systems, coherent scattering is calculated with the use of a recurrent procedure. If a heterostructure consists of N layers, including the substrate, and the coefficient of reflection $R^{\rm c}_{N-1}(q_x, q_z)$ from $(N-1)$ lower layers is known, the amplitude coefficient of reflection from a heterostructure $R^{\rm c}_N(q_x, q_z)$ is computed using the recursive formula [33]

$$R^{\rm c}_N(q_x, q_z) = \frac{S_1^{(N)} b_2^{(N)} - S_2^{(N)} b_1^{(N)}}{S_1^{(N)} - S_2^{(N)}}, \qquad (52)$$

where

$$S_1^{(N)} = \left(R_{N-1}(q_x, q_z) - b_1^{(N)}\right) \exp\left({\rm i}\xi^{(N)} l_N\right),$$

$$S_2^{(N)} = R_{N-1}(q_x, q_z) - b_2^{(N)}, \qquad b_{1,2}^{(N)} = \frac{\xi_{1,2}^{(N)}}{f_N a_{-h}^N},$$

$$\xi_{1,2}^{(N)} = \frac{-q_z^N \pm \xi^{(N)}}{2}, \qquad \xi^{(N)} = \sqrt{(q_z^N)^2 - 4 a_h^N a_{-h}^N f_N^2},$$

$$q_z^N = (1+b) a_0^N + \varepsilon^N h + q_z, \qquad \varepsilon^N = \frac{\Delta d_N}{d_0}$$

is lattice strain in the Nth layer.

Because short-period superlattices with QDs are usually two-component structures, coherent scattering is calculated using formulas (51) and (52). Numerical simulation of diffuse scattering from crystalline media is performed as described in the preceding paragraphs with due regard for the QD size, shape, elastic strain, and spatial correlation.

Quantitative X-ray diffraction analysis was done for a structure analogous to a photoluminescence system with $Al_{0.3}Ga_{0.7}As$ barriers as thick as 2 μm at the bottom and 450 nm at the top, having 240 nm thick upper and lower CaAs waveguides. The 20-period superlattice with repeated wetting (InAs) and spacing (GaAs) layers formed the active region. The structures were grown by molecular beam epitaxy on undoped GaAs(001) substrates. After the removal of arsenic oxide from the substrate surface, the 300 nm thick GaAs buffer layer was grown at 610 °C on which the main structure of interest formed. Quantum dots were deposited at $T = 480$ °C at a rate of ~ 0.035 monolayers per second. The instant of QD formation, with the deposited layer thickness being ~ 1.7 monolayers, was recorded from the appearance of chevrons close to the diffraction spots of reflected electrons [106].

X-ray diffraction measurements were carried out on a high-resolution X'Pert MRD diffractometer (PANalytical). Double- and triple-crystal $(\omega - 2\theta)$ rocking curves (RCs) and triple-crystal ω RCs at the maximum of the main diffraction peaks [GaAs(004), AlGaAs] and superstructural satellites from the multilayer active region (0SL, ±1SL, and others) were measured. RSMs of scattered radiation were recorded with the analyzer crystal in the $(\omega - 2\theta)/\omega$ scanning mode around the symmetric (004) reciprocal lattice node.

A priori growth information was used to construct a model of a 20-period GaAs(001)–AlGaAs–$\{{\rm InAs/GaAs}\}_{20{\rm xSL}}$ structure with InAs QDs. The first stage of the X-ray diffraction analysis consists in numerical simulation of coherent diffraction, because its intensity is much higher than that of the diffuse component [106]. Coherent scattering by multilayer structures is calculated based on analytic solution (51) and recurrent procedure (52) to take diffraction on the substrate and the buffer layer into account. In the case

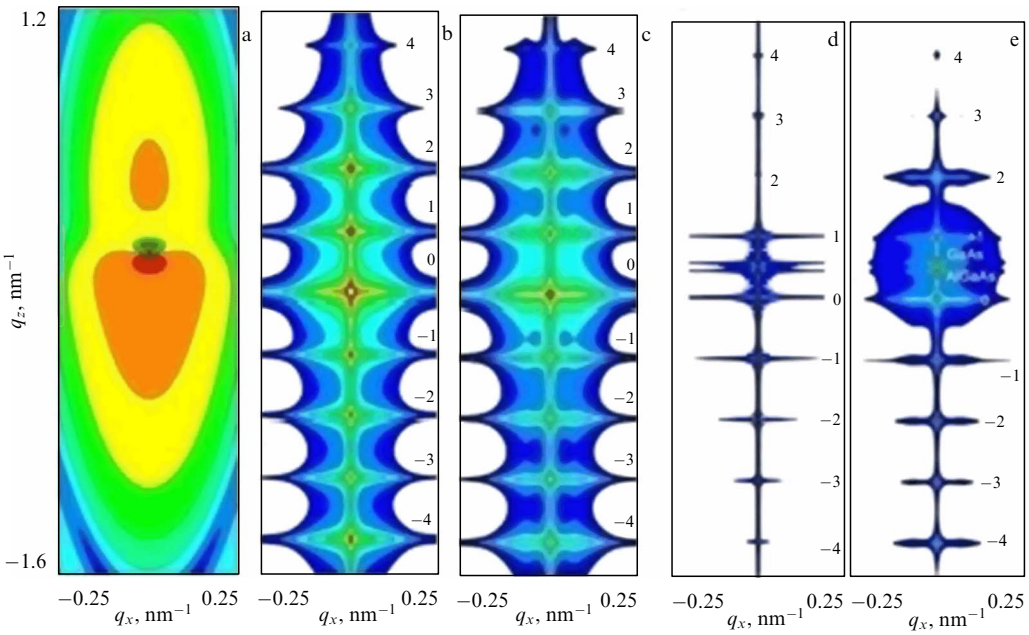

Figure 16. Simulated RSM of (a-c) diffuse and (d) coherent X-ray scattering; (a) the absence of correlation in the QD arrangement, (b) vertical QD correlation, (c) vertical and lateral QD correlation.

under consideration, the numerical simulation of the RSM vertical section is performed for (004)GaAs reflection of σ-polarized $CuK_{\alpha 1}$-radiation. Bragg's angle for the chosen reflection is 33.026°, and the lattice spacing for the GaAs substrate is $d_{004} = 1.4133$ Å. Fourier components of the X-ray polarizability have the values

$$\chi_0^{\mathrm{GaAs}} = (-2.889 + \mathrm{i}\,0.084) \times 10^{-5},$$
$$\chi_h^{\mathrm{GaAs}} = (-1.697 + \mathrm{i}\,0.078) \times 10^{-5},$$
$$\chi_0^{\mathrm{InAs}} = (-2.682 + \mathrm{i}\,0.239) \times 10^{-5},$$
$$\chi_h^{\mathrm{InAs}} = (-1.459 + \mathrm{i}\,0.204) \times 10^{-5}$$

(see Ref. [127] and the *X-Ray Server* website address therein).

The best agreement between simulated and observed coherent scattering is obtained for the following parameters: the thickness of the InAs QD-containing InGaAs layer 5.2 nm, the mean composition on the basis of In 11%, the GaAs spacer thickness 14.8 nm, the lattice parameter disparity $\Delta d = d_{\mathrm{InGaAs}} - d_{\mathrm{GaAs}} = 2.2 \times 10^{-3}$ nm, the elastic strain $\varepsilon = \Delta d / d_{\mathrm{GaAs}} = 0.016$, the static Debye–Waller factor of the InGaAs layer with QDs $f = 0.85$.

The next stage is sequential modeling of diffuse scattering, which requires taking peculiar features of the object of interest into account. The size of self-organized QDs in a semiconducting matrix is known to be different, even if their volume variance is not very large. Nevertheless, numerical simulation of diffuse scattering requires statistical averaging over QD vertical and lateral dimensions, as for porous crystals [128, 129]. Following the formalism in [130], statistical averaging over QD dimensions L can be performed with the use of the lognormal distribution

$$p_{\mathrm{LN}}(L) = \frac{1}{\sqrt{2\pi} L \sigma_{\mathrm{LN}}} \exp\left\{ -\frac{\left[\ln\left(L/\langle L\rangle\right) + \sigma_{\mathrm{LN}}^2/2\right]^2}{2\sigma_{\mathrm{LN}}^2} \right\} \quad (L \geqslant 0),$$

where $\langle L\rangle = \int_0^\infty L p_{\mathrm{LN}}(L)\,\mathrm{d}L$ is the mean QD size in the lateral and vertical dimensions. Then the QD size variance $\sigma_L^2 = \int_0^\infty (L - \langle L\rangle)^2 p_{\mathrm{LN}}(L)\,\mathrm{d}L$ and the position $L_{\max}$ of the maximum in the QD distribution by size are written as

$$\sigma_L^2 = \left[\exp\left(\sigma_{\mathrm{LN}}^2\right) - 1\right] \langle L\rangle^2,$$

$$L_{\max} = \exp\left(-\frac{3\sigma_{\mathrm{LN}}^2}{2}\right) \langle L\rangle.$$

For a small QD size variance, transition to the normal distribution occurs:

$$\sigma_L^2 \cong \sigma_{\mathrm{LN}}^2 \langle L\rangle^2, \qquad L_{\max} \cong \langle L\rangle.$$

Numerical simulation of diffuse scattering begins with a medium model in which the spatial QD correlation is absent. The simplest but adequate enough shape of QDs is chosen for the purpose. This requirement is satisfied by the spheroidal QD model, which is especially simple for statistical averaging over the nanostructure size.

Figure 16a shows a simulated map of the angular distribution of coherent scattering by a 20-period InAs/GaAs superlattice with chaotically arranged ellipsoidal QDs. In this case, QDs in an arbitrary superlattice period are in no way related to the QD distribution in the adjacent layers. The QD lateral radius is $R = 12.5$ nm and the height is $l_z = 5$ nm. In the numerical calculations, the QD lateral density is taken into account, with the distance to the neighboring QD boundary in the horizontal direction being 32.5 nm, corresponding to half the mean QD–QD distance. These structural QD parameters were obtained by direct comparison of theoretical and experimental data.

Figure 16b illustrates the simulated distribution of diffuse scattering from an InAs/GaAs superlattice with only vertical QD correlation included. Since the SL period is strictly maintained to be 20 nm, the QD vertical correlation is described in the framework of a long-range-order model. It follows from Fig. 15 that the vertical correlation strongly influences the width of diffuse maximum bands in the vertical

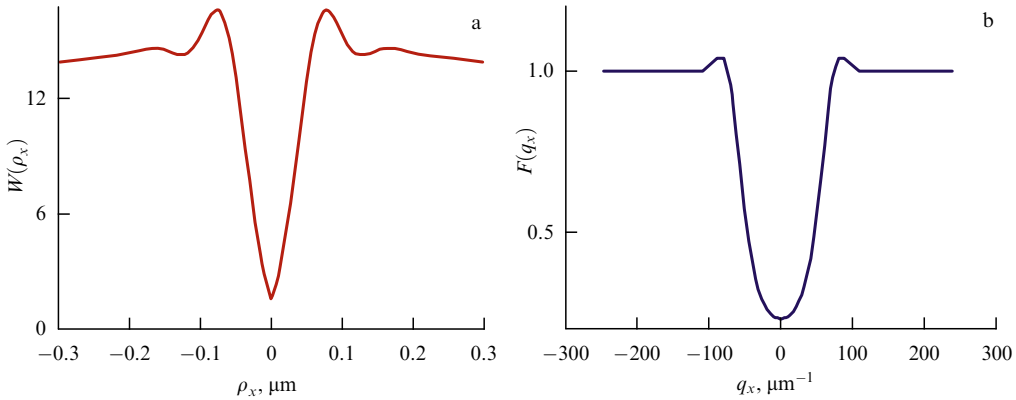

Figure 17. (a) QD distribution function and (b) the interference structural factor for the mean distance between QD centers $a = 65$ nm and the variance $\Delta^a = 0.45a = 29$ nm [106].

direction by decreasing it while increasing the correlation length. A comparison of theoretical and observed characteristics of the structure of interest showed that the QD vertical correlation length is roughly 140 nm, in agreement with the stacking length averaged over the thickness of seven periods of the 20-period superlattice.

Lateral correlation between the nearest QDs was described in terms of the paracrystalline lattice formalism [112] with the introduction of the probability function for the QD location. In the simulated model, the spatially correlated QDs of the InGaAs epitaxial layer form a random square lattice, whose fuzziness is described by the normal (Gaussian) distribution. The QD distribution function $W(\rho_x)$ for the mean distance between QD centers $a = 65$ nm and variance $\Delta^a = 0.45a = 29$ nm are presented in Fig. 17a. The corresponding interference structural factor

$$F_{\mathrm{L}}(q_x) = \int F_{\mathrm{L}}(q_x, q_y)\,\mathrm{d}q_y$$

is shown in Fig. 17b. The influence of vertical and lateral correlations on the distribution of diffuse scattering from QDs is demonstrated in Fig. 16c. The mean distance between QDs and the corresponding variance were obtained by direct comparison of theoretical and experimental data.

A comparative analysis of the experimental and calculated RSM section curves was based on minimizing the residual functional

$$\rho = \frac{1}{M}\sum_{m=1}^{M}\left[\frac{I_{\mathrm{exp}}(q_{x,z}^m) - I_{\mathrm{calc}}(q_{x,z}^m)}{I_{\mathrm{exp}}(q_{x,z}^m)}\right]^2, \qquad (53)$$

where $I_{\mathrm{exp}}(q_{x,z}^m)$ is the measured intensity at angular positions q_x^m for an ω scan and q_z^m for an $(\omega{-}2\theta)$ scan, $I_{\mathrm{calc}}(q_{x,z}^m)$ is the corresponding calculated total scattering intensity, and M is the number of angular positions at which scattered radiation was collected. In our calculations, $M = 50$ for ω scans and $M = 460$ for $(\omega{-}2\theta)$ scans. Minimization of the residual functional was carried out for ω scans of all superlattice satellites. The discrepancy between theory and experiment was about 5%.

In the first approximation of numerical calculations of coherent scattering (Fig. 16d), the lateral width of the incident X-ray beam and its angular divergence were described by the pseudo-Voigt function [131, 132]. Therefore, the total intensity (Fig. 16e) was the result of adding diffuse (Fig. 16c) and coherent (Fig. 16d) scattering. A more accurate numerical calculation requires taking the instrumental function of experimental studies into account (Fig. 18c).

Figure 18 shows experimental and simulated maps of the distribution of radiation scattering by a 20-period GaAs(001)–AlGaAs–$\{$InAs(QDs)/GaAs$\}_{20\mathrm{xSL}}$ superlattice near the GaAs(004) reciprocal lattice node. Calculations of the total intensity of scattering by the substrate and the buffer layer took the influence of defects into account in the framework of dislocation models [133, 134]. The best quantitative agreement between experimental and theoretical ω and $(\omega{-}2\theta)$ scans was obtained for the values of the Debye–Waller factor of the substrate $f_{\mathrm{s}}^{\mathrm{subs}} = 0.96$ and of the AlGaAs-buffer layer $f_{\mathrm{s}} = 0.94$. We note that such agreement was impossible to reach in calculations of diffuse scattering without taking the QD stacking length into consideration [135].

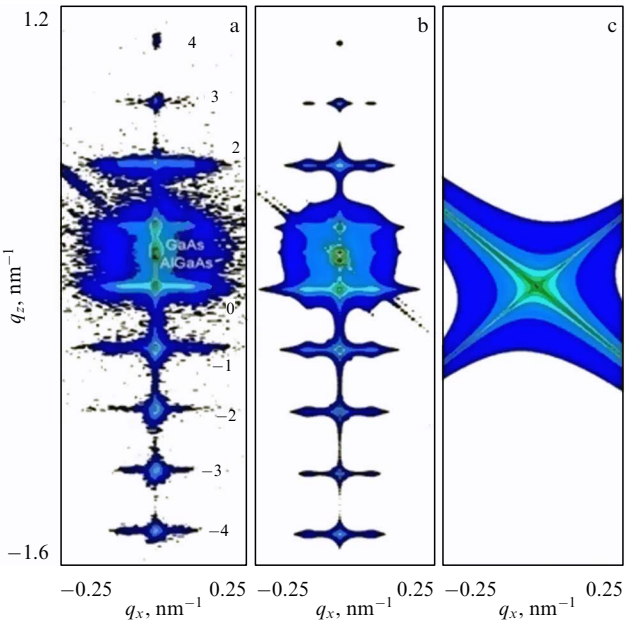

Figure 18. (a) Experimental and (b) simulated RSMs from a 20-period GaAs(001)–AlGaAs–$\{$InAs(QDs)/GaAs$\}_{20\mathrm{xSL}}$ superlattice near the GaAs(004) reciprocal lattice node. (c) The presence of the analyzer strip on the simulated map is due to the consideration of instrumental measurement function.

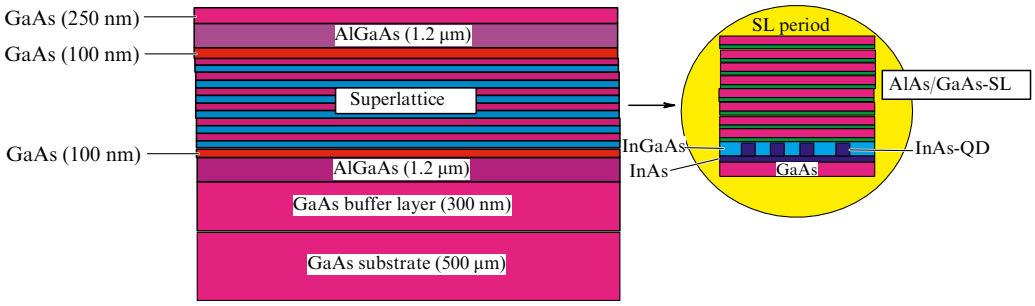

Figure 19. Schematic of a heterostructure with the multicomponent superlattice. Right panel: the structure of the period of a superlattice with QDs [125].

The calculation shows that the static factor is $f_{QD} = \exp(-c_{QD}V_{QD}) = 0.927$, where $V_{QD} = (3\pi/2)R^2 l_z = 1.6 \times 10^{-6}$ μm^3 is the mean QD volume without taking elastic strain into account, $R = 12.5$ nm is the mean QD lateral radius, the mean QD height is $l_z = 5$ nm (vertical size), and $c_{QD} = 4.7 \times 10^4$ μm^{-3} is the bulk QD concentration in the InGaAs layer of the superlattice period corresponding to the mean QD concentration in the layer $\sim 2.4 \times 10^{10}$ cm^{-2}. The concentration c_{QD} was calculated using the QD height and the mean distance between QD centers $a = 65$ nm (the mean area of an individual QD $S_{QD} = a^2 = 4225$ nm^2; therefore, the mean surface concentration of QDs is $\rho_{QD}^S = 1/S_{QD} = 2.367 \times 10^{10}$ cm^{-2}). The calculated total static Debye–Waller factor for the InGaAs layer was $f = f_{QD}f_s = 0.85$. The static Debye–Waller factor due to elastic strain and defects near QDs corresponding to this value was $f_s = 0.917$. Averaging over QD dimensions smooths the influence of the nanostructure shape on diffuse scattering. In this case, the main structural characteristic of QDs is the $\eta = h/D$ ratio [102], where h is the QD height and D its diameter. For the structure of interest, $\eta = 0.2$.

6.2 Multicomponent heterostructures with quantum dots

Interlayer QD correlations in multilayer structures obey a certain mechanism by which the QDs of one layer affect QD growth in the next one, i.e., information about QD positions is transferred from one layer to another. There are three types of such mechanisms: segregation chemical processes at the surface, morphological peculiarities of the undulated surface, and long-range interactions of elastic strain fields from QDs [136, 137]. Each of these processes causes changes in strain, surface diffusion, and the surface chemical potential across the spacer. If these changes are sufficiently large, they affect nucleation of subsequent QDs and thereby give rise to vertical and lateral correlations in multilayer systems.

Nucleation of QDs via the Stranski–Krastanov growth mode is a complicated process depending on a variety of parameters, such as the surface tension, the lattice mismatch, the wetting layer thickness and composition, the free energy and local growth surface curvature, the stepped surface structure, and growth kinetics. On a planar and chemically homogeneous surface, these parameters are constant over the surface width; this results in the nucleation of individual dots at random positions on the surface. In multilayer structures, variations in the strain and chemical composition caused by overgrown QDs lead to selective QD nucleation at specific positions on the surface. As a result, QDs on this surface become spatially correlated with respect to the dots in the preceding layers; in this way, the interlayer QD correlation is formed [137].

Spacer thickness is paramount for the formation of vertically coupled QD arrays. As is known, the interlayer QD correlation decreases with the spacer thickness [138, 139]. Following [125, 126], we discuss coherent and diffuse scattering by superlattices with QDs in the presence of a relatively thick multicomponent spacer. The laser-type GaAs(001)–GaAs–AlGaAs–AlAs heterostructures being studied were grown by molecular beam epitaxy on precisely oriented (001)GaAs substrates. They are schematically depicted in Fig. 19.

The main $Al_xGa_{1-x}As$ (thickness $t \approx 1.2$ μm) and GaAs ($t \approx 100$ nm) layers, as well as thin GaAs and AlAs layers in smoothing short-period ($t_{SL} \approx 3.6$ nm) superlattices were grown at $\approx 600\,^\circ$C, whereas InAs QDs and GaAs layers immediately adjacent to them (≈ 5 nm below and ≈ 2.5 nm above) were deposited at $\approx 480\,^\circ$C; the arsenic flow was reduced several-fold during QD deposition by means of a regulator on a valved cracker. The InAs deposition rate was $\approx 0.03-0.032$ monolayers per second.

To enhance the vertical QD size homogeneity, the substrate temperature was increased to $\approx 600\,^\circ$C to remove the protruding upper part of QDs [140]. Then the thickness of the GaAs layer was built up to ≈ 5.0 nm to enable formation of a smoothing short-period AlAs (1.1 nm)/GaAs (2.5 nm) superlattice composed of 9 layer pairs. The total number of periods with InAs QDs in the examined superstructures was 3, 6, and 10; the overall period of the layers with QDs was ≈ 54 nm for the first two samples (3 and 6 periods) and ≈ 48 nm for the third one (10 periods).

X-ray diffractometry was done with a high-resolution X′Pert MRD (PANalytical) diffractometer with a multilayer focusing mirror, a four-bounce Ge(220) Bartels monochromator providing a divergence of the incident radiation of about 12 arcsec, and a three-bounce Ge(220) analyzer with the receiver angular aperture of about 7–8 arcsec. The use of the X-ray optical scheme with the Bartels monochromator ensured high monochromatization and collimation of the incident $CuK_{\alpha 1}$ radiation, while the high-resolution analyzer allowed spatial separation of coherent and diffuse components of the scattered radiation to obtain detailed information about the crystal perfection of the studied objects. GaAs(004) reflection was used to measure $(\omega-2\theta)$ and ω RCs and the maps of scattering intensity distribution around the reciprocal lattice node.

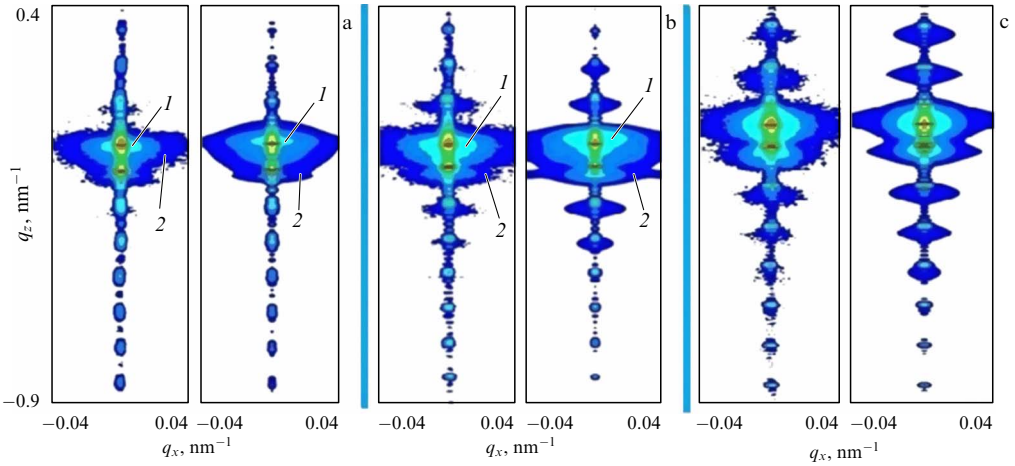

Figure 20. (Color online). Experimental (left) and simulated RSMs near the (004) GaAs reciprocal lattice node containing (a) three, (b) six, and (c) ten periods of superlattice structures with quantum dots [125, 126]. *1* — light blue regions, *2* — dark blue regions.

RSM calculations were done by the above method with minimization of the residual functional [53].

Figure 20 shows observed and simulated RSMs for samples containing 3, 6, and 10 periods with QDs. The appearance of coherent and diffuse diffraction orders on the light blue (regions *1*) and dark blue (regions *2*) RSMs is quite apparent. For the three-period superlattice, diffuse scattering from QDs is poorly manifested due to the small number of layers with QDs (Fig. 20a), whereas the other two samples exhibit a conspicuous angular shift of diffraction spots of incoherent scattering relative to coherent peaks (Fig. 20b, c) [125, 126].

Strictly speaking, all models considered previously [141–146] and the available experimental data [69, 75–77, 147] gave evidence of X-ray diffuse scattering by modulated disfigured crystals, including superlattices with QDs initiated in the immediate vicinity of superstructural satellites of coherent scattering. The first results on the shift of diffuse scattering maxima by a certain angular distance with respect to coherent superstructural satellites were reported in [125, 126]. An explanation of this previously unknown effect is proposed in Ref. [125].

According to (46) and (47), the diffuse scattering distribution in RSs is a periodic function along the q_z section. The period of diffuse maxima arrangement $K = 2\pi/l_{\mathrm{SL}}$ coincides with the period of coherent diffraction orders. X-ray radiation is coherently scattered by all P layers of the superlattice period, with the coherent component in the imperfect superlattice regions being weaker due to a decrease in the static Debye–Waller factor. According to Bragg's law $2d_{\mathrm{SL}} \sin\theta^{\mathrm{c}}_{\mathrm{SL}} = \lambda$, the mean lattice spacing $d_{\mathrm{SL}} = \sum_{p=1}^{P} d_p l_p / l_{\mathrm{SL}}$ determines the angular position $\theta^{\mathrm{c}}_{\mathrm{SL}}$ of the main (zeroth) superlattice diffraction peak. Satellite maxima in the reciprocal space are shifted by the angular distances nK, where n is the diffraction order number.

Diffuse scattering does not occur in the absence of defects in the layers of a heterostructure. It is produced only in QD-containing layers and in the neighboring ones into which the QD-induced elastic strain penetrates. A multicomponent lattice may contain fewer layers than the superlattice period (P). Let the number of layers with defects in which diffuse scattering occurs be S and $S \leqslant P$. Then the mean lattice spacing in the superlattice for diffuse scattering can be written as $d^{\mathrm{D}}_{\mathrm{SL}} = \sum_{s=1}^{S} d_s l_s / l^{\mathrm{D}}_{\mathrm{SL}}$ [125, 148], where $l^{\mathrm{D}}_{\mathrm{SL}} = \sum_{s=1}^{S} l_s$ is the thickness of the defective part of the superlattice period. In the general case, $d^{\mathrm{D}}_{\mathrm{SL}}$ may be different from the mean lattice spacing d_{SL} in the superlattices for coherent scattering. By virtue of the same Bragg's law, $2d^{\mathrm{D}}_{\mathrm{SL}} \sin\theta^{\mathrm{D}}_{\mathrm{SL}} = \lambda$, where $\theta^{\mathrm{D}}_{\mathrm{SL}}$ is the angular position of the zeroth diffuse scattering maximum. The angular shift between coherent and diffuse scattering maxima around the RL node on an RSM is determined by the relation $\Delta q_{\mathrm{SL}} = h^{\mathrm{D}}_{\mathrm{SL}} - h_{\mathrm{SL}}$, where $h^{\mathrm{D}}_{\mathrm{SL}} = 2\pi/d^{\mathrm{D}}_{\mathrm{SL}}$ and $h_{\mathrm{SL}} = 2\pi/d_{\mathrm{SL}}$ [125].

When QD-induced elastic strains are distributed across all layers of the superlattice period, i.e., $P = S$, the mean lattice spacings for coherent and diffuse scattering coincide, $d_{\mathrm{SL}} = d^{\mathrm{D}}_{\mathrm{SL}}$; therefore, the diffraction order maxima of these two scattering channels also coincide, $\Delta q_{\mathrm{SL}} = 0$. This case is realized for homogeneous thin spacers. As a result, a shift between coherent and diffuse scattering maxima is absent [106].

A comparison of theoretical and experimental RSMs shows that diffuse scattering maxima are shifted by $\Delta q_{\mathrm{SL}} = 0.025$ nm^{-1}, which means that diffuse scattering originates not in the entire superlattice period thickness but only in the part containing QDs and the QD-induced elastic strain. The results of calculations suggest that in the case of a six-period superlattice, induced strain spreads over 40 nm in the growth direction, the period thickness being 54 nm. In the case of a 10-period SL, this distance is 32 nm (the period thickness is 48 nm). The multicomponent spacer prevents the formation of good stacked QD arrays. Unlike short-period superlattices, where the mean stacking length encompasses seven periods [106], the QD vertical correlation length in multicomponent heterostructures is roughly equal to two superlattice periods with the variance of a quarter of the period. Thus, only two vertically coincident QDs are present in a multicomponent superlattice.

Numerical simulations yielded the QD sizes. The mean QD height was 2.5 nm, and the mean lateral size was 20 nm. The variance of the QD sizes fluctuations in the vertical and lateral directions was 30%. Diffraction analysis of multicomponent superlattices revealed long-range order in the lateral arrangement of QDs. The mean distance between QDs was 50 nm, and the variance was 20 nm.

7. Conclusion

This review presents a step-by-step description of nondestructive X-ray diffraction research on semiconducting systems with QDs for the purpose of quantitative RSM analysis. This topic is of paramount importance because the HRXRD method with RSM measurements is used to study new systems with QDs. Results of RSM analysis, anomalous X-ray diffraction, high-resolution TEM, and photoluminescence spectroscopy have recently been used to characterize the structural and optical properties of GaN/AlN superlattices with QDs [149]. Vertical QD correlation in a ZnTe/ZnCdSe system was studied with the use of a lateral deviation model [120] for the analysis of diffraction orders on RSMs [150, 151].

A difficulty encountered in quantitative RSM analysis arises from the fact that experimental scattering intensity distribution maps contain very large arrays of data (from 100 to 1000 values in each direction on a two-dimensional grid, which roughly corresponds to a range from ten thousand to one million intensity values on the RSM). The problem is simplified if only selected RSM sections are considered. For each intensity value, it is necessary either to make analytic calculations or to numerically solve multistep integral and differential equations. Because the fitting method implies multiple repetition of calculations, the solution of the inverse problem of X-ray diffraction is hardly possible without the use of supercomputers.

We recall that RSM calculations for differently shaped QDs were made in the framework of alternative approaches. Specifically, X-ray scattering from buried QDs was simulated in the framework of the kinematic theory with the use of a finite-element algorithm and the valence force field model (Keating model) for the elastic strain energy [152, 153]. But the use of the kinematical approximation to calculate diffraction from the volume part in these studies is not quite correct due to dynamical diffraction for a large number of atoms, regardless of the crystal shape [154].

Weak angular deviation of diffuse scattering from coherent satellites at the vertical RSM sections was described for InAs/GaAs [155, 156] and Ge/Si [157] superlattices with QDs. Unfortunately, the authors of these publications do not provide a definitive explanation of this phenomenon.

One more important remark is in order as regards research with the use of HRXRD but without mapping, i.e., without RSM measurements [158–171]. In many such cases, additional measurements are needed, e.g., of diffuse scattering [157] and photoluminescence spectra [158, 160, 163, 164, 168–171], as well as the use of TEM [161, 162, 168–171) and AFM [169]. Clearly, related experiments yield additional information about systems with QDs. On the other hand, double-crystal RCs alone are hardly sufficient, for instance, to identify pyramidal InAs QDs in superconducting heterostructures or to draw a conclusion on the vertical coupling (stacking) of QDs without an analysis of diffuse scattering [165–167].

The approach described in this review can be effectively used for quantitative analysis of other classes of nanostructured media, e.g., for the study of self-organized quantum wires [172] and those obtained by lithographic techniques [173–175], laterally bounded crystals of different shapes [176–180], multilayer diffraction gratings [181], laterally modulated superlattices [182, 183], thin layers with quasiperiodic dislocations [184], domain [185, 186] and porous [187–190] structures, etc.

This work was supported in part by the RFBR (project No. 13-02-00272-a).

References

1. Wang Z M (Ed.) *Self-Assembled Quantum Dots* (New York: Springer, 2008)
2. Alferov Zh I *Rev. Mod. Phys.* **73** 767 (2001); *Usp. Fiz. Nauk* **172** 1068 (2002)
3. Arakawa Y, Sakaki H *Appl. Phys. Lett.* **40** 939 (1982)
4. Goldstein L et al. *Appl. Phys. Lett.* **47** 1099 (1985)
5. Bimberg D (Ed.) *Semiconductor Nanostructures* (Berlin: Springer, 2008)
6. Blokland J H et al. *Appl. Phys. Lett.* **94** 023107 (2009)
7. Pavlov K M, Punegov V I, Faleev N N *JETP* **80** 1090 (1995); *Zh. Eksp. Teor. Fiz.* **107** 1967 (1995)
8. Punegov V I, Faleev N N *Phys. Solid State* **38** 143 (1996); *Fiz. Tverd. Tela* **38** 255 (1996)
9. Punegov V I et al. *Phys. Solid State* **38** 148 (1996); *Fiz. Tverd. Tela* **38** 264 (1996)
10. Renaud G, Lazzari R, Leroy F *Surf. Sci. Rep.* **64** 255 (2009)
11. Holý V, Buljan M, Lechner R T *Semicond. Sci. Technol.* **26** 064002 (2011)
12. Favre-Nicolin V et al. *Eur. Phys. J. Special Topics* **208** 189 (2012)
13. Chrastina D et al. *Nanotechnology* **23** 155702 (2012)
14. Vartanyants I A et al. *Phys. Rev. B* **71** 245302 (2005)
15. Schmidbauer M *X-Ray Diffuse Scattering from Self-Organized Mesoscopic Semiconductor Structures* (Berlin: Springer, 2004)
16. Pietsch U, Holý V, Baumbach T *High-Resolution X-ray Scattering: from Thin Films to Lateral Nanostructures* (New York: Springer, 2004)
17. Als-Nielsen J, McMorrow D *Elements of Modern X-ray Physics* (Hoboken: Wiley, 2011)
18. Caciuffo Ret al. *Phys. Rep.* **152** 1 (1987)
19. Bonse U, Hart M *Appl. Phys. Lett.* **7** 238 (1965)
20. Compton A H, Allison S K *X-ray in Theory and Experiment* (New York: D. Van Nostrand Co., 1935)
21. Eisenberger P, Alexandropoulos N G, Platzman P M *Phys. Rev. Lett.* **28** 1519 (1972)
22. Larson B C, Schmatz W *Phys. Rev. B* **10** 2307 (1974)
23. Iida A, Kohra K *Phys. Status Solidi A* **51** 533 (1979)
24. Fewster P F, Andrew N L *J. Phys. D Appl. Phys.* **28** A97 (1995)
25. Gartstein E, Mandelbrot M, Mogilyanski D *J. Phys. D Appl. Phys.* **34** A57 (2001)
26. Godwod K, Żymierska D, Auleytner J *J. Phys. D Appl. Phys.* **36** A148 (2003)
27. Nesterets Ya I, Gureyev T E, Wilkins S W *J. Phys. D Appl. Phys.* **38** 4259 (2005)
28. Kato N *Acta Cryst. A* **36** 763 (1980)
29. Bushuev V A *Sov. Phys. Crystallogr.* **34** 163 (1989); *Kristallogr.* **34** 279 (1989)
30. Bushuev V A *Sov. Phys. Solid State* **31** 1877 (1989); *Fiz. Tverd. Tela* **31** (11) 70 (1989)
31. Punegov V I *Sov. Phys. Crystallogr.* **35** 336 (1990); *Kristallogr.* **35** 576 (1990)
32. Punegov V I, Petrakov A P, Tikhonov N A *Phys. Status Solidi A* **122** 449 (1990)
33. Punegov V I *Phys. Status Solidi A* **136** 9 (1993)
34. Punegov V I, Vishnjakov Y V *J. Phys. D Appl. Phys.* **28** A184 (1995)
35. Punegov V I, Kharchenko A V *Cryst. Rep.* **43** 1020 (1998); *Kristallogr.* **42** 1078 (1998)
36. Pavlov K M, Punegov V I *Acta Cryst. A* **54** 214 (1998)
37. Pavlov K M, Punegov V I *Acta Cryst. A* **56** 227 (2000)
38. Nesterets Y I, Punegov V I *Acta Cryst. A* **56** 540 (2000)
39. Punegov V I, Lomov A A, Shcherbachev K D *Phys. Status Solidi A* **204** 2620 (2007)
40. Punegov V I, Nesterets Y I, Roshchupkin D V *J. Appl. Cryst.* **43** 520 (2010)
41. Holý V *Phys. Status Solidi B* **111** 341 (1982)
42. Holý V *Phys. Status Solidi B* **112** 161 (1982)
43. Dederichs P H *Phys. Rev. B* **4** 1041 (1971)

44. Krivoglaz M A *X-Ray and Neutron Diffraction in Nonideal Crystals* (Berlin: Springer, 1996); Translated from Russian: *Difraktsiya Rentgenovskikh Luchei i Neitronov v Neideal'nykh Kristallakh* (Kiev: Naukova Dumka, 1983)
45. Bushuev V A *Phys. Solid State* **37** 136 (1995); *Fiz. Tverd. Tela* **37** 249 (1995)
46. Takagi S *Acta Cryst.* **15** 1311 (1962)
47. Punegov V I *Tech. Phys. Lett.* **38** 523 (2012); *Pis'ma Zh. Tekh. Fiz.* **38** (11) 53 (2012)
48. Punegov V I *Crystallogr. Rep.* **58** 663 (2013); *Kristallogr.* **58** 652 (2013)
49. Bushuev V A "Uglovoe raspredelenie intensivnostei dinamicheskoi difraktsii rentgenovskikh luchei v kristallakh s mikrodefektami v geometriyakh Laue i Bregga" ("The distribution of dynamic X-ray diffraction intensities in crystals with microdefects in Laue and Bragg geometry"), Dep. VINITI No. 486-B88 (Moscow: VINITI, 1988)
50. Punegov V I *Crystallogr. Rep.* **54** 391 (2009); *Kristallogr.* **54** 423 (2009)
51. Punegov V I, Sivkov D V, Klad'ko V P *Tech. Phys. Lett.* **37** 364 (2011); *Pis'ma Zh. Tekh. Fiz.* **37** (8) 41 (2011)
52. Punegov V I, Sivkov D V *Tech. Phys. Lett.* **39** 964 (2013); *Pis'ma Zh. Tekh. Fiz.* **39** (21) 60 (2013)
53. Punegov V I *Tech. Phys. Lett.* **35** 20 (2009); *Pis'ma Zh. Tekh. Fiz.* **35** (1) 41 (2009)
54. Goncharskii A V, Kolpakov A V, Stepanov A A *Obratnye Zadachi Rentgenovskoi Difraktometrii* (Inverse Problems of X-ray Diffractometry) (Riga: Latviiskii Univ., 1992)
55. Podorov S G, Punegov V I, Kusikov V A *Phys. Solid State* **36** 454 (1994); *Fiz. Tverd. Tela* **36** 827 (1994)
56. Podorov S G, Punegov V I *Tech. Phys.* **44** 299 (1999); *Zh. Tekh. Fiz.* **69** (3) 39 (1999)
57. Krasil'nikov A G, Punegov V I, Faleev N N *Tech. Phys. Lett.* **30** 489 (2004); *Pis'ma Zh. Tekh. Fiz.* **30** (12) 6 (2004)
58. Chuev M A, Lomov A A, Imamov R M *Crystallogr. Rep.* **51** 178 (2006); *Kristallogr.* **51** 208 (2006)
59. Sutyrin A G, Imamov R M *Crystallogr. Rep.* **56** 57 (2011); *Kristallogr.* **56** 61 (2011)
60. Volkov Yu O et al. *Crystallogr. Rep.* **58** 160 (2013); *Kristallogr.* **58** 146 (2013)
61. Bushuev V A, Sergeev A A *Tech. Phys. Lett.* **25** 83 (1999); *Pis'ma Zh. Tekh. Fiz.* **25** (3) 1 (1999)
62. Holý V, Pietsch U, Baumbach T *High-Resolution X-Ray Scattering from Thin Films and Multilayers* (Berlin: Springer, 1999)
63. Darhuber A A et al. *Europhys. Lett.* **32** 131 (1995)
64. Darhuber A A et al. *Physica B* **227** 11 (1996)
65. Holý V et al. *Phys. Rev. B* **52** 8348 (1995)
66. Holý V et al. *Solid-State Electron.* **40** 373 (1996)
67. Darhuber A A et al. *Phys. Rev. B* **58** 4825 (1998)
68. Baribeau J-M *J. Cryst. Growth* **157** 52 (1995)
69. Darhuber A A et al. *Phys. Rev. B* **55** 15652 (1997)
70. Holý V et al. *Phys. Rev. B* **58** 7934 (1998)
71. Darhuber A A et al. *Physica E* **2** 789 (1998)
72. Bauer G, Darhuber A A, Holý V *Cryst. Res. Technol.* **34** 197 (1999)
73. Darhuber A A et al. *Appl. Phys. Lett.* **70** 955 (1997)
74. Darhuber A A et al. *Thin Solid Films* **306** 198 (1997)
75. Faleev N et al. *Jpn. J. Appl. Phys.* **38** 818 (1999)
76. Faleev N N et al. *Semiconductors* **33** 1229 (1999); *Fiz. Tekh. Poluprovodn.* **33** 1359 (1999)
77. Faleev N N et al. *Semiconductors* **35** 932 (2001); *Fiz. Tekh. Poluprovodn.***35** 969 (2001)
78. Holý V et al. *Physica B* **283** 65 (2000)
79. Springholz G et al. *Appl. Phys. Lett.* **82** 799 (2003)
80. Lechner R T et al. *Appl. Phys. Lett.* **84** 885 (2004)
81. Díaz B et al. *Nanotechnology* **23** 015604 (2012)
82. Oshima R et al. *J. Cryst. Growth* **301 – 302** 776 (2007)
83. Manna U et al. *J. Appl. Phys.* **111** 033516 (2012)
84. Schmidbauer M et al. *Phys. Rev. Lett.* **96** 066108 (2006)
85. Hanke M et al. *Appl. Phys. Lett.* **94** 203105 (2009)
86. Shoji Y et al. *Physica E* **42** 2768 (2010)
87. Kladko V P et al. *Phys. Status Solidi A* **204** 2567 (2007)
88. Kladko V et al. *Phys. Status Solidi A* **206** 1748 (2009)
89. Novák J et al. *J. Appl. Phys.* **98** 073517 (2005)
90. Grützmacher D et al. *Nano Lett.* **7** 3150 (2007)
91. Holý V et al. *Phys. Rev. B* **79** 035324 (2009)
92. Maranganti R, Sharma P, in *Handbook of Theoretical and Computational Nanotechnology* Vol. 1 (Eds M Rieth, W Schommers) (New York: Am. Sci. Publ., 2005) Ch. 118, p. 1
93. Benabbas T, Androussi Y, Lefebvre A *J. Appl. Phys.* **86** 1945 (1999)
94. Daruka I et al. *Phys. Rev. B* **60** R2150 (1999)
95. Yang M, Xu S J, Wang J *Appl. Phys. Lett.* **92** 083112 (2008)
96. Andreev A D et al. *J. Appl. Phys.* **86** 297 (1999)
97. Nenashev A V, Dvurechenskii A V *J. Appl. Phys.* **107** 064322 (2010)
98. Yang M, Sturm J C, Prevost J *Phys. Rev. B* **56** 1973 (1997)
99. Aqua J-N et al. *Phys. Rep.* **522** 59 (2013)
100. Maia A D B et al. *J. Phys. D Appl. Phys.* **45** 225104 (2012)
101. Punegov V I, Kolosov S I, Pavlov K M *Tech. Phys. Lett.* **32** 809 (2006); *Pis'ma Zh. Tekh. Fiz.* **32** (18) 65 (2006)
102. Hesse A et al. *Phys. Rev. B* **66** 085321 (2002)
103. Ulloa J M et al. *Phys. Rev. B* **81** 165305 (2010)
104. Ulloa J M, Bozkurt M, Koenraad P *Solid State Commun.* **149** 1410 (2009)
105. Ulloa J M et al. *J. Appl. Phys.* **112** 074311 (2012)
106. Faleev N N, Honsberg C, Punegov V I *J. Appl. Phys.* **113** 163506 (2013)
107. Zernike F, Prins J A *Z. Phys.* **41** 184 (1927)
108. Hosemann R *Z. Phys.* **128** 465 (1950)
109. Punegov V I *Sov. Tech. Phys. Lett.* **18** 120 (1992); *Pis'ma Zh. Tekh. Fiz.* **18** (4) 66 (1992)
110. Punegov V I *Izv. Komi Nauch. Tsentra Ural'sk. Otd. Ross. Akad. Nauk* (1) 11 (2010)
111. Pal D, Towe E, Chen S *Appl. Phys. Lett.* **78** 4133 (2001)
112. Punegov V I *Tech. Phys. Lett.* **37** 696 (2011); *Pis'ma Zh. Tekh. Fiz.* **37** (15) 8 (2011)
113. Buljan M et al. *Phys. Rev. B* **79** 035310 (2009)
114. Schmidbauer M, Hanke M, Köhler R *Phys. Rev. B* **71** 115323 (2005)
115. Kegel I et al. *Appl. Phys. Lett.* **74** 2978 (1999)
116. Bushuev V A *J. Surf. Invest. X-ray Synchrotron Neutron Tech.* **1** 522 (2007); *Poverkhnost. Rentgen. Sinkhron. Neitron. Issled.* (9) 29 (2007)
117. Eads J L, Millane R P *Acta Cryst. A* **57** 507 (2001)
118. Punegov V I, Lomov A A *Tech. Phys. Lett.* **34** 238 (2008); *Pis'ma Zh. Tekh. Fiz.* **34** (6) 30 (2008)
119. Pukite P R, Lent C S, Cohen P I *Surf. Sci.* **161** 39 (1985)
120. Kegel I et al. *Phys. Rev. B* **60** 2516 (1999)
121. Punegov V I *Tech. Phys. Lett.* **39** 475 (2013); *Pis'ma Zh. Tekh. Fiz.* **39** (10) 54 (2013)
122. Steward E G *Fourier Optics: An Introduction* (Chichester: E. Horwood, 1983)
123. Köhler R et al., in *Semiconductor Nanostructures* (Ed. D Bimberg) (Berlin: Springer, 2008) p. 97
124. Punegov V I, Nesterets Ya I *Tech. Phys. Lett.* **20** 674 (1994); *Pis'ma Zh. Tekh. Fiz.* **20** (16) 62 (1994)
125. Punegov V I, Faleev N N *JETP Lett.* **92** 437 (2010); *Pis'ma Zh. Eksp. Teor. Fiz.* **92** 483 (2010)
126. Punegov V I, Faleev N N *Bull. Russ. Acad. Sci. Phys.* **75** 36 (2011); *Izv. Ross. Akad. Nauk Ser. Fiz.* **75** 42 (2011)
127. Stepanov S, Forrest R *J. Appl. Cryst.* **41** 958 (2008)
128. Lomov A A et al. *Crystallogr. Rep.* **55** 182 (2010); *Kristallogr.* **55** 196 (2010)
129. Punegov V I, Lomov A A *Tech. Phys. Lett.* **36** 122 (2010); *Pis'ma Zh. Tekh. Fiz.* **36** (3) 60 (2010)
130. Boulle A, Conchon F, Guinebretière R *Acta Cryst. A* **62** 11 (2006)
131. Ida T, Ando M, Toraya H *J. Appl. Cryst.* **33** 1311 (2000)
132. Punegov V I *Tech. Phys.* **57** 37 (2012); *Zh. Tekh. Fiz.* **82** (1) 40 (2012)
133. Kaganer V M et al. *Phys. Rev. B* **55** 1793 (1997)
134. Kaganer V M, Sabelfeld K K *Acta Cryst. A* **70** 457 (2014)
135. Punegov V I *Tech. Phys. Lett.* **34** 864 (2008); *Pis'ma Zh. Tekh. Fiz.* **34** (20) 8 (2008)
136. Springholz G *Comptes Rendus Physique* **6** 89 (2005)
137. Springholz G, Holý V, in *Lateral Alignment of Epitaxial Quantum Dots* (Ed. O Schmidt) (Berlin: Springer, 2007) p. 247
138. Xie Q et al. *Phys. Rev. Lett.* **75** 2542 (1995)
139. Legrand B et al. *Appl. Phys. Lett.* **74** 2608 (1999)
140. Wasilewski Z R, Fafard S, McCaffrey J P *J. Cryst. Growth* **201 – 202** 1131 (1999)

141. Punegov V I *Sov. Phys. Solid State* **32** 1438 (1990); *Fiz. Tverd. Tela* **32** 2476 (1990)
142. Punegov V I, Pavlov K M *Crystallogr. Rep.* **38** 602 (1993); *Kristallogr.* **38** (5) 34 (1993)
143. Holý V et al. *Superlattices Microstruct.* **12** 25 (1992)
144. Punegov V I *Crystallogr. Rep.* **41** 196 (1996); *Kristallogr.* **41** 246 (1996)
145. Nesterets Ya I, Punegov V I *Crystallogr. Rep.* **44** 382 (1999); *Kristallogr.* **44** 422 (1999)
146. Nesterets Ya I, Punegov V I *Crystallogr. Rep.* **44** 913 (1999); *Kristallogr.* **44** 980 (1999)
147. Nesterets Ya I et al. *Tech. Phys.* **44** 171 (1999); *Zh. Tekh. Fiz.* **69** (2) 44 (1999)
148. Punegov V I *Phys. Met. Adv. Technol.* **5** 33 (2010); *Metallofiz. Noveish. Tekhnol.* **32** 33 (2010)
149. Leclere C et al. *J. Appl. Phys.* **113** 034311 (2013)
150. Dhomkar S et al. *Appl. Phys. Lett.* **103** 181905 (2013)
151. Dhomkar S et al. *Solar Energy Mater. Solar Cells* **117** 604 (2013)
152. Rawle J L, Howes P B *Surf. Rev. Lett.* **10** 525 (2003)
153. Rawle J L, Howes P B *Eur. Phys. J. Spec. Topics* **167** 47 (2009)
154. Authier A *Dynamical Theory of X-Ray Diffraction* (New York: Oxford Univ. Press, 2001)
155. Klad'ko V P et al. *Metallofiz. Noveish. Tekhnol.* **26** 1255 (2004)
156. Mazur Yu I et al. *J. Appl. Phys.* **99** 023517 (2006)
157. De Seta M et al. *J. Appl. Phys.* **102** 043518 (2007)
158. Krost A et al. *Appl. Phys. Lett.* **68** 785 (1996)
159. Krost A et al. *Appl. Phys. Lett.* **75** 2957 (1999)
160. Xu S et al. *Appl. Phys. Lett.* **77** 2130 (2000)
161. Pal D et al. *J. Cryst. Growth* **233** 34 (2001)
162. Pal D, Towe E, Chen S J *Appl. Phys. Lett.* **78** 4133 (2001)
163. Wang H et al. *Chin. Phys. Lett.* **18** 810 (2001)
164. Krishna S et al. *Appl. Phys. Lett.* **80** 3898 (2002)
165. Pashaev E M et al. *Phys. Status Solidi A* **195** 204 (2003)
166. Pashaev E M et al. *Russ. Microelectron.* **31** 310 (2002); *Mikroelektron.* **31** 367 (2002)
167. Zaitsev A A et al. *Russ. Microelectron.* **33** 27 (2004); *Mikroelektron.* **33** 35 (2004)
168. Huang X-Q et al. *J. Cryst. Growth* **270** 364 (2004)
169. Tatebayashi J et al. *J. Phys. D Appl. Phys.* **42** 073002 (2009)
170. Bailey C G et al. *Appl. Phys. Lett.* **95** 203110 (2009)
171. Carrington P J et al. *Physica B* **407** 1493 (2012)
172. Holy V et al. *Phys. Rev. B* **63** 205318 (2001)
173. Darhuber A A et al. *J. Phys. D Appl. Phys.* **28** A195 (1995)
174. Baumbach T, Lubbert D, Gailhanou M *J. Appl. Phys.* **87** 3744 (2000)
175. Punegov V I *Poverkhnost. Rentgen. Sinkhrotron. Neitron. Issled.* (1) 77 (2002)
176. Kolosov S I, Punegov V I *Crystallogr. Rep.* **50** 375 (2005); *Kristallogr.* **50** 401 (2005)
177. Punegov V I et al. *Tech. Phys. Lett.* **32** 809 (2006); *Pis'ma Zh. Tekh. Fiz.* **32** (18) 65 (2006)
178. Punegov V I, Kolosov S I *Crystallogr. Rep.* **52** 191 (2007); *Kristallogr.* **52** 215 (2007)
179. Punegov V I et al. *Tech. Phys. Lett.* **33** 125 (2007); *Pis'ma Zh. Tekh. Fiz.* **33** (3) 64 (2007
180. Punegov V I, Kolosov S I, Pavlov K M *Acta Cryst. A* **70** 64 (2014)
181. Punegov V I *Tech. Phys. Lett.* **30** 1 (2004); *Pis'ma Zh. Tekh. Fiz.* **30** (1) 3 (2004)
182. Li J H et al. *Phys. Rev. B* **66** 115312 (2002)
183. Li J H et al. *J. Appl. Phys.* **107** 123504 (2010)
184. Wintersberger E et al. *Appl. Phys. Lett.* **96** 131905 (2010)
185. Bazzan M et al. *J. Appl. Phys.* **106** 104121 (2009)
186. Roshchupkin D V, Irzhak D V, Antipov V V *J. Appl. Phys.* **105** 024112 (2009)
187. Lomov A A et al. *Crystallogr. Rep.* **57** 185 (2012); *Kristallogr.* **57** 232 (2012)
188. Punegov V I *Tech. Phys. Lett.* **38** 523 (2012); *Pis'ma Zh. Tekh. Fiz.* **38** (11) 53 (2012)
189. Punegov V I *Crystallogr. Rep.* **58** 663 (2013); *Kristallogr.* **58** 652 (2013)
190. Lomov A A et al. *J. Appl. Cryst.* **47** 1614 (2014)